HERON is jointly edited by:
STEVIN-LABORATORY of the
faculty of Civil Engineering,
Delft University of Technology,
Delft, The Netherlands
and
TNO BUILDING AND
CONSTRUCTION RESEARCH.
Rijswijk (ZH), The Netherlands
HERON contains contributions
based mainly on research work
performed in these laboratories on
strength of materials, structures
and materials science.

ISSN 0046-7316

Secretary:
J. G. M. van Mier
Stevinweg 1
P.O. Box 5048
2600 GA Delft, The Netherlands
Tel. 0031-15-784578
Fax 0031-15-786993
Telex 38151 BUTUD

HERON vol. 39
1994
no. 1

Contents

LONG-DISTANCE ULTRASONIC TESTING OF STEEL STRUCTURES

D. J. Chinn
Lawrence Livermore National Laboratory
Mechanical Engineering Department
Livermore, California 94550
USA

formerly: Delft University of Technology,
Faculty of Civil Engineering

Publication in HERON since 1970

Long-distance ultrasonic testing of steel structures

1 Introduction

1.1 *Background*

Achieving an acceptable level of reliability over the lifetime of a structure requires a consistent strategy of integrity assessment, repair and maintenance. The structures as well as their environments determine the requirements on these three operations. While repair and maintenance operations are rarely easy in any environment, the method with which they are accomplished is fairly straightforward. Integrity assessment, in contrast, can be accomplished in a variety of ways.

An integrity assessment evaluates the need for repairs and in addition yields information on the remaining useful life of a structure. Integrity is assessed by measuring the extent of damage which reduces the expected structural performance. Most commonly, damage occurs during the lifetime of the structure and assessment takes place during use. In addition, damage can occur during fabrication. Defective construction also reduces performance and requires integrity assessment before use for damage during fabrication .

Many non-destructive testing (NDT) methods have been developed for measuring damage of large steel structures such as offshore installations, bridges, rails, pressure vessels and sluice gates. For these types of structures the primary types of damage that can potentially degrade performance are fabrication defects and cracks due to cyclic loading. An NDT method assesses the integrity of the structure, either before or during its useful lifetime, without causing damage to it. NDT may be divided into methods that involve *inspection* and methods that involve *monitoring*. In the context of this thesis, the terms are generally defined such that inspection techniques concern crack or defect characterization while monitoring techniques look at changes in the behavior of the structure or component under loading.

NDT methods can result in *detection*, *location* and/or *characterization* of a defect in a structure. These results are listed in increasing levels of sensitivity. Detection, the lowest level of sensitivity, entails simply determining the existence of a defect in a structure or component that is not included in its design. Location of a defect, possible after its detection, pinpoints the area of the defect's existence. Characterization of a defect, possible only after it has been detected and located, reveals its type, form or dimensions. Each NDT method has a different sensitivity level in different applications.

Common inspection techniques of large steel structures include visual inspection, magnetic particle inspection, radiography, ultrasonic inspection and electrical loss methods. (Chinn 1989) These methods have the capability of characterizing small and large-sized cracks and defects with varying degrees of sensitivity. Inspection measurements are reproducible and are often recorded for periodic documentation purposes. Most structures in use today rely on a combination of these inspection types.

All of the inspection methods target small, selected areas of a structure and are performed by qualified inspectors. As such, these methods are labor-intensive. Because of the localized nature of inspection methods, they require close-range accessibility to suspect areas. Most integrity assessment requirements on large structures can be satisfied with the present capabilities of inspection methods. Although inspection techniques are time-consuming, labor-intensive and as a result expensive, they still provide the only means of detailed characterization of defects. New developments and current research on inspection methods are concerned mainly with economization of inspection time.

Monitoring methods have recently received much attention due to the high costs of inspection. These methods perform integrity testing of a structure without an inspector or remotely-operated-vehicle (ROV) physically being at the point of assessment. Monitoring techniques usually only require long-range accessibility to suspect areas. This characteristic feature decreases the risk of further damage to critical areas and can also lower the cost of testing hidden or inaccessible connections.

Monitoring methods for large steel structures include acoustic emission testing, vibration analysis, and strain history measurement. Relative to inspection methods, monitoring methods assess large areas of a structure with a single set of measurements. While quite successful in detecting and locating most large types of defects, the global nature of monitoring renders it incapable of detecting small defects or characterizing any defect on a detailed level. Changes in global behavior of the structure indicate more extensive damage than detected by inspection methods.

Monitoring methods have certain limitations in tracking fatigue crack growth. On a tubular offshore structure, the sensitivity of vibration analysis is limited to the detection and general location of cracks with length longer than approximately 20% of the member circumference. (Lepert 1980) Acoustic emission and strain history monitoring, while more sensitive than vibration analysis, require that the structure be under stress in order to determine crack existence and growth and are therefore not reproducible.

Monitoring methods try to economize, not replace, inspection methods. Analysis of monitoring data identifies possible defect locations and can sometimes characterize a defect in broad terms. Monitoring methods routinely require follow-up inspection to determine the actual severity and the exact location of a flaw. The intention of monitoring is to guide the assessment to suspect areas, thereby efficiently using inspection time.

1.2 *Purpose and related work*

A void exists between the capabilities of inspection and monitoring. The goal of this research is to develop a hybrid method which ideally incorporates the advantages of both inspection and monitoring. Economically, a hybrid method should allow localized inspection without extensive operations. This can be accomplished by testing large global areas with one set of measurements as in monitoring methods. Operations are facilitated if the hybrid method requires only long-range accessibility. With respect to performance, a hybrid method should detect, locate and characterize a full range of defects including small cracks, through-wall cracking and extensive longitudinal and circumferential crack-

ing. In this way, fatigue crack growth can be tracked and repaired as necessary. For reliability, data from a hybrid method should be recordable and reproducible.

Table 1. 1. Features of inspection and monitoring can be combined to produce a hybrid method of testing. The features in the shaded boxes are those desired in a hybrid method.

Feature	*Inspection*	*Monitoring*
testing area	localized	global
accessibility	close-range	long-rang
sensitivity level	characterization of small and large defects	location of large defects
reproducibility	requires constant conditions in local test area	global conditions affect measurements
expense	labor-intensive	analysis-intensive

Table 1.1 lists the features of both inspection and monitoring techniques. Those features desired in a hybrid method that combine advantages of inspection and monitoring are shaded in the table. Obviously, the relative importance of each feature varies with the application. However a hybrid method should provide the potential for the combination of inspection and monitoring features in any application.
Recent work on hybrid techniques in steel satisfying the requirements set out in Table 1.1 all use guided Lamb waves (Redwood 1960; Viktorov 1967) for defect detection. Lamb waves, also called plate waves, use the cross-section of the member as a waveguide. Lamb wave generation physically requires that the plate or wall thickness be on the order of the wavelength of excitation. Slow in attenuating, this type of wave can be used to assess large areas as in monitoring. A pulsed Lamb wave can radiate throughout a large part of a structure. By varying the input signal, detection and location of small flaws is possible as with inspection methods.

1.3 *Scope*

This study develops a potential hybrid method that combines the advantages of both inspection and monitoring on thick steel members where detection, location, and estimation of severity is required. The primary application targets large-scale civil engineering structures subject to cyclic loading. In these types of structures critical areas are generally located near welded steel connections. Fatigue cracks in these areas are usually surface-breaking and grow normal to the direction of high stress. In many cases these fatigue cracks grow in a plane. The sensitivity required for detection of fatigue crack initiation and growth can only be achieved using small wavelengths, i.e. high frequency wave propagation. Lamb waves were previously thought to be the only means of propagating a high frequency wave packet over long distances without severe attenuation. In this study,

it is shown that ultrasonic bulk waves can be used over a distance of at least 2.0 m to and from a defect while maintaining sufficient assessment information.
A secondary application of the technique concerns evaluation of steel components during fabrication. Testing in this application involves looking for defects in both weld and base material. Fabrication testing generally involves the assessment of large areas, not specifically limited to points of high stress as in cyclically-loaded structures.
The technique developed, long-distance ultrasonic testing, uses existing ultrasonic testing methods to evaluate an area within approximately 1.0 m. This is a departure from present ultrasonic testing methods where testing occurs within 0.1–0.3 m from a suspect area. Because larger areas of a structure may be evaluated from a farther distance than with normal ultrasonic testing, economical features of a monitoring method are realized. The testing distance permits long-range accessibility to critical areas. Using frequencies in the 1–10 MHz range allows sensitivity to fatigue-induced cracks sized on the order of 3–5 mm in length and can detect growth. Present close-range ultrasonic inspection techniques have been shown to provide excellent characterization of defects in steel. (Lorenz 1991; Lorenz 1993) In place of the characterization derived from labor-intensive close-range inspection, this work develops an analytical model to aid in characterization from the large testing distance.

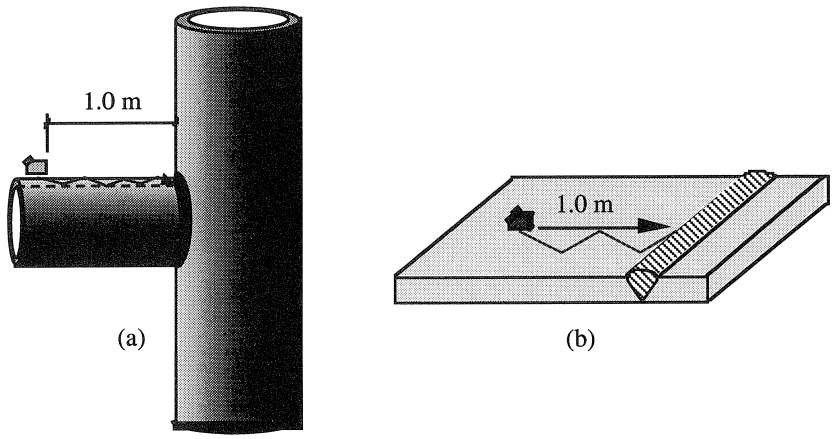

Fig. 1.1. Long-distance ultrasonic testing applied to (a) a tubular steel connection and (b) steel plate fabrication testing.

Fig. 1.1 shows possible applications of long-distance ultrasonic testing to a tubular steel connection and to the fabrication of a steel plate. Large steel structures having connections as shown in Fig. 1.1a typically have wall or member thicknesses of 20–40 mm. The frequency range used in long-distance ultrasonic testing assures that bulk waves propagate in steel members of this thickness. From 1.0 m testing distance, a bulk wave must reflect several times before reaching the test area at the connection. Using an angled probe to generate the bulk wave maximizes the energy that reaches the test area. In the presence of a defect the wave reflects from the defect face and propagates back to the

probe. The plate in Fig. 1.1b also has thickness of ~20 mm. Long-distance testing uses a single measurement to assess a 1.0 m distance of structure.

2 Long-distance ultrasonic measurement techniques

2.1 *Measurement system*

Fig. 2.1 shows the ultrasonic measurement system used and characterized in this chapter. The pulser initiates the measurement process as indicated by the arrows. The Metrotek MP 217 square wave pulser generates electronic signals at a repetition rate of 500 Hz. A pulse sent to the probe triggers both the receiver and the recorder on the IBM AT. The chosen pulse duration optimizes the signal emanating from the probe. The term probe refers to the component that converts the electrical signal to mechanical excitation in the steel specimen and vice versa. Probes used in long-distance testing consist of a transducer and a 70° wedge. The wedge directs the energy into the steel at an angle. Piezoelectric elements in the transducers perform the conversion between electrical and mechanical energy. All interfaces transferring mechanical energy use gel couplant to provide continuous displacement across the interface. A thin layer of couplant fills the transducer-wedge and wedge-steel interfaces.

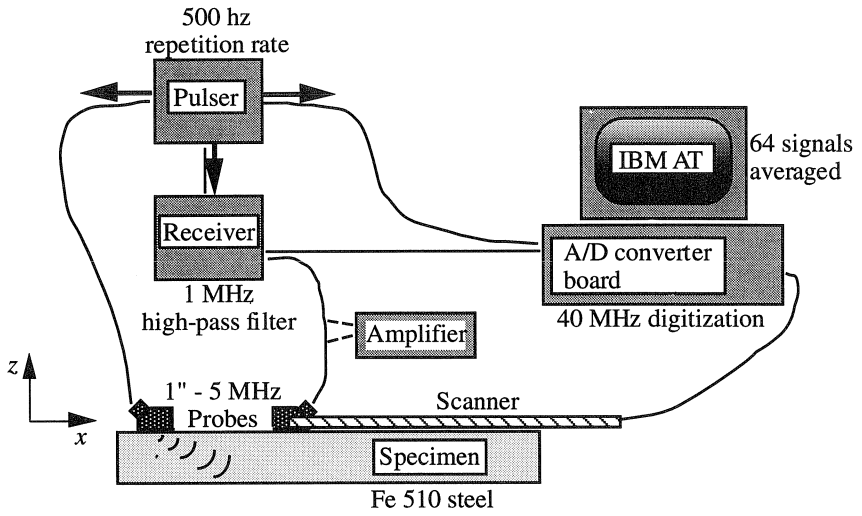

Fig. 2.1. General measurement setup for ultrasonic testing.

Mechanical traction produced by the probe generates a wave field in the specimen. The receiving probe converts the mechanical response in the specimen back to electrical energy sending the response signal to the receiver/amplifier. Electrical signals from the receiver are related to the velocity response in the specimen at the receiving probe.
The receiver has a high-pass filter removing most of the frequency components in the signal below 1 MHz. In addition, the receiver amplifies the signal up to +60 decibels

[dB]. At large offset distances between the sending and receiving probes, the amplifier increases the received signal by an extra +40 dB amplifier.
The Waag II 8-bit analog-to-digital (A/D) converter, located on a board in the IBM AT, digitizes the electrical signal from the receiver at a rate of 40 MHz. This provides sufficient sampling of the 5 MHz signal from the probe to prevent aliasing of the specimen response. In addition to the signal obtained from the response of the specimen, each electrical signal contains some amount of random noise disturbance contributed by the electrical system. To reduce this noise, the IBM AT averages 64 signals. This increases the signal-to-noise (S/N) ratio by a factor of 8. (Cooper, C.D. 1971) The hard disk of the computer stores the digitized, averaged response. An example signal collected with the measurement is shown in Fig. 2.2.

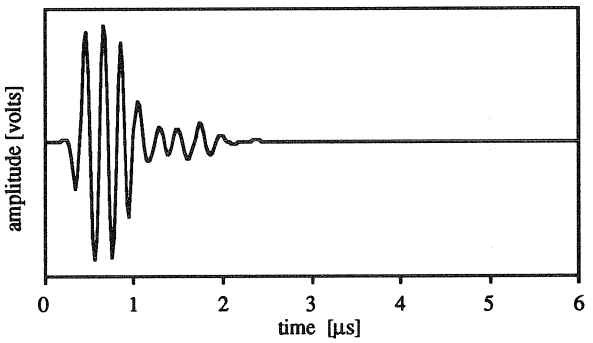

Fig. 2.2. Sample signal collected at 40 MHz and averaged 64 times.

The AT controls an x-direction scanner which moves the receiving probe linearly along the surface of the specimen. Scanning enables the observation of the specimen response at different offsets from the source. The scanning system raises and lowers the receiving probe before measuring from the next offset position. During measurement, the scanner applies a constant pneumatic pressure of 1.5 bars to the receiving probe in the z-direction.

2.2 *Probe characterization*

An ultrasonic probe is chosen on the basis of its application. In long-distance testing, the probe must send a packet of energy through a steel member, illuminating the entire thickness up to 1 m away. The energy packet should reflect from both small and large defects, after which it must propagate back through the plate to a receiving probe. Minimization of losses during wave propagation maximizes the energy received.
Pulsed energy packets help distinguish between different wave paths. A continuous or long-duration signal does not provide sufficient resolution to the arriving waves in the received response. In addition pulsed signals, having a distribution of frequencies, avoid possible harmonic resonance in the plate.
A highly directional source delivers the maximum illumination energy to the area of testing and has a minimum amount of spreading in the wave field. Losses due to spreading of the wave field decrease the energy available for reflection from a defect.

Propagation over long-distances with bulk waves using a surface source requires several reflections from the plate faces. At a free surface, an incident *P*-wave always generates both a *P* and an *S*-wave. An incident *S*-wave generates only a reflected *S*-wave when the angle of incidence θ_0 satisfies $\theta_0 > \theta_{cr}$, where θ is the angle of wave propagation measured from the normal to the surface. The critical angle θ_{cr} is approximately 32° in steel. Above this angle, *S*-waves reflect at an amplitude and angle equal to the incident *S*-wave. To prevent mode conversion from *S* to *P*-waves at the plate surface, the probe generates *S*-waves with propagation angle larger than θ_{cr}. When propagating *S*-waves larger than the critical angle, an *S*-wave remains an *S*-wave even after multiple reflections from the plate surface. Using a large angle for *S*-wave propagation angle further minimizes the number of reflections and the propagation path length in a plate. A 70° *S*-wave is chosen for long-distance propagation in the steel medium.

For long-distance testing measurements, a 1" diameter contact transducer with 5 MHz center frequency mounted on a perspex wedge is used to generate 70° *S*-waves in steel. A 5 MHz center frequency results in an *S*-wavelength of $\lambda_s = 0.6$ mm, sufficiently small to detect fatigue cracks on the order of 5 mm. Commercially available wedges commonly use perspex because of its durability and transmission properties. The transducer generates *P*-waves in the perspex which, when incident on a perspex-steel interface, produce *S*-waves in the steel as shown in Fig. 2.3.

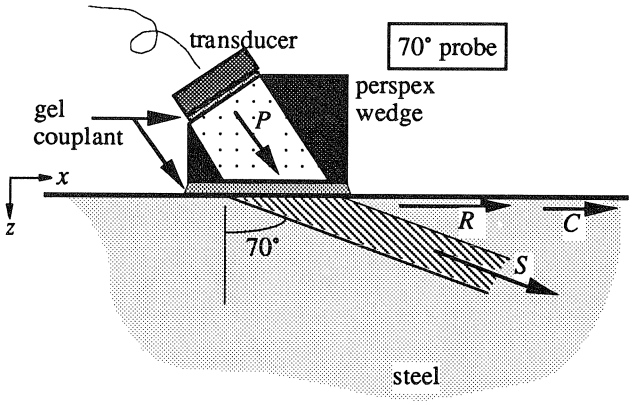

Fig. 2.3. Probe components for 70° ultrasonic *S*-wave generation.

A thin layer of gel couplant effectively transfers the *z*-component of *P*-waves from the perspex to the steel. (Kühn, Lutsch 1961) Mode conversion occurs at the boundary producing an *S*-wave in the steel. Edge effects of the probe generate a surface creeping (*C*) wave and a Rayleigh (*R*) wave. (Krautkrämer, Krautkrämer 1990) The *C*-wave travels along the surface with the same speed as a longitudinal wave but loses energy quickly. The *R*-wave can travel relatively large distances along the plate surface before dissipating.

2.3 *Measured wave propagation in steel*

The 1"–5 MHz probe is designed for testing of steel such that 70° waves result. This section presents the attenuation properties of the wave field in steel produced by the probe. Two types of attenuation influence long-distance testing of steel. Apparent attenuation due to beam diffraction depends on the source geometry and the medium. Attenuation due to energy dissipation results from the dissipative properties of the medium. Attenuation losses generally increase with propagation distance and as a result determine the primary limitations of long-distance testing. The magnitudes of both types of attenuation depend on frequency. Measurements produced by scanning the plate reveal the changes in the wave field resulting from the two types of attenuation.

2.3.1 Diffraction spreading

Diffraction attenuation results from interference effects of a finite-sized source on the surface of a medium. Larger diameters and higher frequencies increase source directionality.

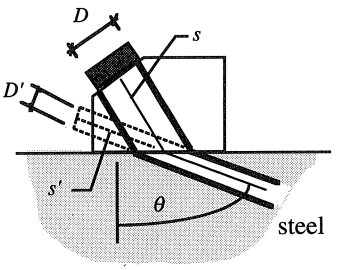

Fig. 2.4. Model of virtual source for an *S*-wave angled probe.

To characterize spreading in the medium due to the 70° probe, we transform the probe and the probe-steel interface into an equivalent virtual surface source (Wüstenburg, Schulz 1977). The virtual source creates an equivalent diffracted *S*-wave field as shown in Fig. 2.4. From laws of refraction the diameter of the virtual source, D' is

$$D' = \frac{D\cos\theta}{\sqrt{1-\left(\frac{c_P - \text{wedge}}{c_S - \text{steel}}\sin\theta\right)^2}} \tag{2.1}$$

The equivalent wave path through the wedge determines the distance between the virtual source and the steel interface, s'. The equivalent path through the wedge is inversely proportional to the wave velocities of the two interfacing media.

$$s' = s\left(\frac{c_P - \text{wedge}}{c_S - \text{steel}}\right) \tag{2.2}$$

For the 1", 70° *S*-wave probe, D' = 14.5 mm and s' = 22.1 mm. The wave velocities used in these calculations are $c_{P\text{-}wedge}$ = 2730 m/s for the perspex and $c_{S\text{-}steel}$ = 3200 m/s for the steel.

The near-field is a region in front of a finite source characterized by an absolute lack of spreading in the wave field. The near-field of the probe along the propagation path extends 30.5 mm into the steel at 3 MHz. On-axis in the near-field, i.e. along the near-field 70° wave path, no diffraction effects are measured for same-sized sending and receiving probes.

Outside the near-field, a circular source generates lobes of varying pressure. Maxima and minima in the wave field result from the interference pattern of the source. Fig. 2.5 shows the directivity pattern for the 70° probe. One main lobe of high pressure is centered at 70°.

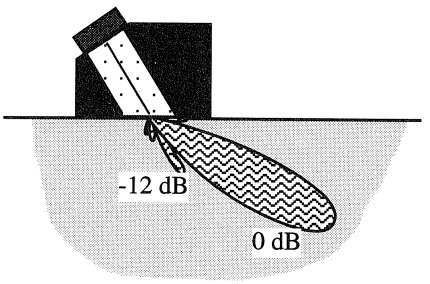

Fig. 2.5. 70° probe far-field directivity on steel.

Within the main lobe the pressure varies with angle. Maximum far-field pressure occurs on the 70° axis of the probe. Specific angles of divergence in the main lobe signify the deviation of pressure from the on-axis maximum. At angle $\gamma_{-6\,dB}$ the pressure decreases to 1/2 of its on-axis maximum. (Krautkrämer, Krautkrämer 1990) For a circular probe with diameter *D*

$$\sin\gamma_{-6dB} = 0.70\frac{\lambda}{D} \tag{2.3}$$

The 70° probe with virtual diameter D' = 14.7 mm has $\gamma_{-6\,dB} \approx 3°$ at 3 MHz and $\gamma_{-6\,dB} \approx 9°$ at 1 MHz (λ_S = 3.2 mm). Fig. 2.6 shows the near-field and the –6 dB range at 1–3 MHz and at 3 MHz.

An inverse relationship occurs between spreading and frequency. At lower frequencies the wave field spreads more than at higher frequencies. At -6 dB the 3 MHz portion of the signal propagates like a pencil ray spreading between 67°–73° while the 1 MHz portion of the signal will spread profusely allowing more ray paths.

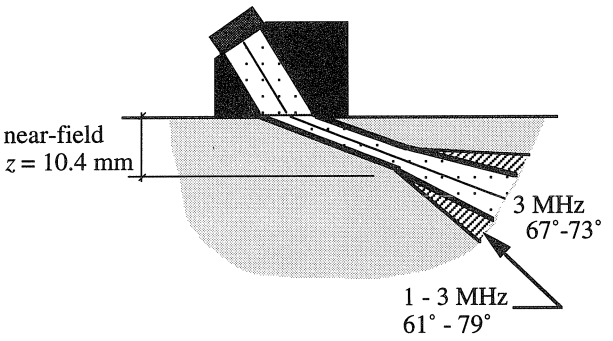

Fig. 2.6. Near-field and far-field –6 dB spreading of 70° probe.

2.3.2 Scattering attenuation

Scattering attenuation in granular solids increases with the grain size of a solid. In steel, the mean grain size $\bar{D}$ ranges from 0.18 mm for coarse-grained cast steel to 0.02 mm for fine-grained annealed steel (Van Vlack 1977). Rayleigh scattering, with an f^4 rate of frequency dependence ($f = c_S / \lambda$), should characterize the attenuation of 1–5 MHz *S*-waves in steel (λ_S = 0.6 – 3.2 mm). This section shows scattering attenuation measurements of *S*-wave propagation in Fe 510 steel.

Fig. 2.7 shows the locations of the probe used to measure attenuation in a plate. The term A_0 denotes the pulsed input signal from the probe. Responses at B_1, B_2, B_3 and B_4 measure 70° through-transmission on a 35 mm thick plate after 0, 1, 2 and 3 reflections respectively.

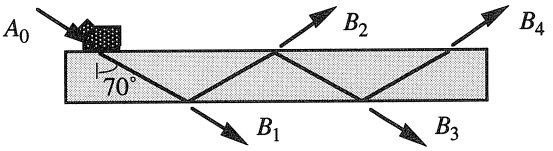

Fig. 2.7. Attenuation measurements of a 70° *S*-wave after 0, 1, 2, and 3 reflections from the plate surface.

Plate surface reflections do not affect the frequency content of a wave. Ignoring diffraction effects and surface roughness, the frequency spectrum of a wavefront at two different propagation distances l_1 and l_2 from a pulsed probe source A_0 is described by (Generazio 1985)

$$\begin{aligned} |B_1(\omega)| &= |A_0(\omega)|\,(1-R^2)\exp[-\alpha(\omega)\,l_1] \\ |B_2(\omega)| &= |A_0(\omega)|\,(1-R^2)\exp[-\alpha(\omega)\,l_2] \end{aligned} \tag{2.4}$$

where $|A_0(\omega)|$ is the Fourier transform of the source and R is the reflection coefficient of the wedge-steel interface. The quantity $(1–R^2)$ represents the net transmission of the wave into and out of the steel at the sending and receiving probes respectively. The absolute

value of the attenuation coefficient $\alpha(\omega)$ is measured by comparing two different output signals with the relation:

$$\alpha(\omega) = \frac{20}{l_2 - l_1} \log \frac{|B_1(\omega)|}{|B_2(\omega)|} \tag{2.5}$$

The units of $\alpha(\omega)$ calculated in this way are [dB/length].
The measurements lie outside the near-field and on the axis of the virtual probe. Including a correction factor for spherical spreading of the wave field by the inverse of distance

$$\frac{p_{B_1}}{p_{B_2}} \cong \frac{z_{B_1}}{z_{B_2}} = \frac{l_2 + s'}{l_1 + s'}$$

to include diffraction effects resulting from the probe-steel interface in eqn. (2.5) gives

$$\alpha(\omega) = \frac{20}{l_2 - l_1} \log \left(\frac{|B_1(\omega)|}{|B_2(\omega)|} \times \frac{l_2 + s'}{l_1 + s'} \right) \tag{2.6}$$

Attenuation in solids is commonly expressed in [dB/mm].

Fig. 2.8 shows the frequency spectra for the B_1, B_2, B_3 and B_4 measurements. The propagation distances, 102.3, 204.6, 306.8 and 409.3 mm, respectively, far exceed the near-field range of the 1" probe. The spectra show frequency-dependent attenuation losses that increase with longer propagation distances. As expected, attenuation increases with frequency.

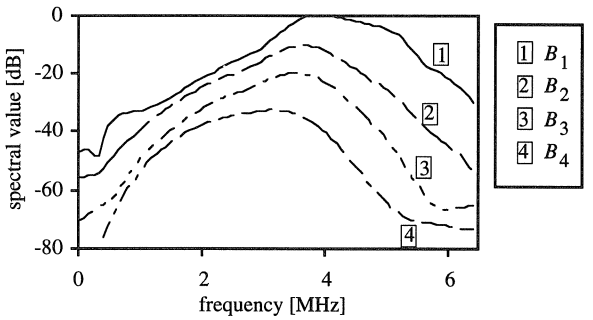

Fig. 2.8. Frequency spectra of measurements B_1, B_2, B_3 and B_4.

Comparing B_1 to each of the other 3 measurements using eqn. (2.6) gives the measured attenuation. Fig. 2.9 shows the attenuation from 3 comparisons of B_1 along with the comparison of B_2 and B_3. The spectra in Fig. 2.8 indicate that the valid region of the attenuation curves (based on 8-bit A/D data conversion) ranges from approximately 1.5–5 MHz.

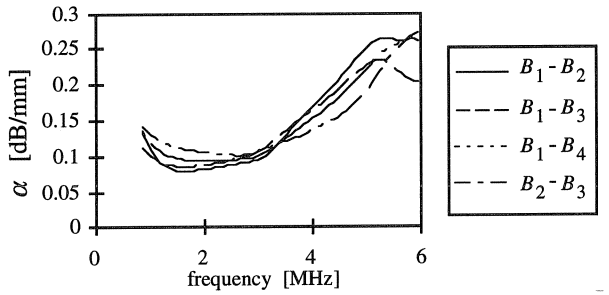

Fig. 2.9. Attenuation $\alpha(\omega)$ of Fe 510 from comparison of B_1-B_2, B_1-B_3, B_1-B_4 and B_2-B_3.

The attenuation at 3 and 5 MHz of *S*-waves in Fe 510 steel is $\alpha_{3\text{ MHz}} = 0.10$ dB/mm and $\alpha_{5\text{ MHz}} = 0.20$ dB/mm. The agreement of the 4 curves in Fig. 2.9 confirms that free-surface reflections do not affect attenuation.

Fig. 2.10 shows the shape of stochastic spreading, $\alpha(f^2)$, between 1–5 MHz. The f^2 relationship of the measured attenuation in the 3–5 MHz range indicates stochastic scattering instead of the expected f^4 Rayleigh scattering. From curve fitting, the attenuation in the range 3–5 MHz is described by

$$\alpha_{3-5\text{ MHz}}(f^2) = 0.035 + 0.0073 f^2 \tag{2.7}$$

where α is expressed in [dB/mm] and f in [MHz]. From 1.5–3 MHz, the attenuation relationship appears in a transition phase. The attenuation remains relatively constant at

$$\alpha_{1.5-3\text{ MHz}} = 0.1\text{ dB/mm} \tag{2.8}$$

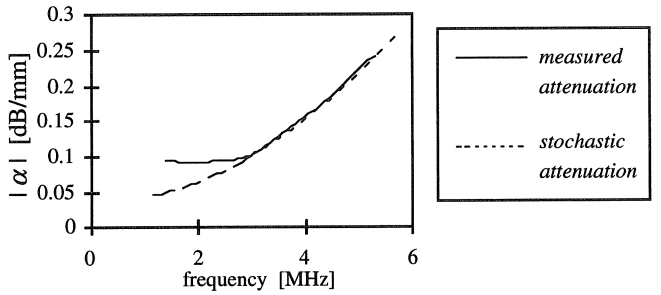

Fig. 2.10. Stochastic $\alpha(f^2)$ relationship on average measured attenuation curve.

The stochastic attenuation behavior may be caused by pearlite inhomogeneities in the steel. More tests are required to confirm this.

2.3.3 Pulsed wave propagation in steel

The previous sections describe the characteristics of the wave field. Diffraction of the field, resulting from the size and shape of the source probe, and scattering, resulting from

inhomogeneities in the Fe 510 steel, both contribute to attenuation behavior during wave propagation. This section compares the measured wave field with the field predicted by the diffraction and scattering models presented earlier, examining the relative importance of each type of attenuation with respect to long-distance testing.

Measurements at intervals of probe offset show the change in the wave field with propagation distance. Fig. 2.11a shows scanning of a 40 mm thick plate with a "through-transmission" configuration. In this configuration, two 70° *S*-wave probes face each other on one side of the specimen. The sending probe generates a wave that travels through the specimen. The receiving probe detects the wave field. This through-transmission configuration is commonly used in ultrasonic testing to detect defects as in Fig. 2.11b. A defect located in the path between the two probes influences the response at the receiving probe.

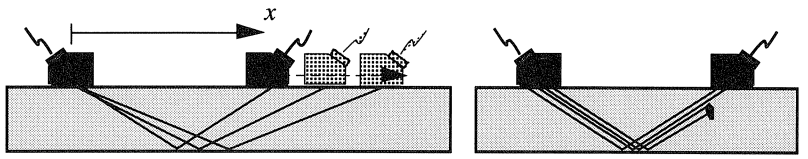

Fig. 2.11. Through-transmission testing (a) with scanning to characterize the wave field and (b) for detection of defects.

The specimen used to characterize the wave field has no defects. Without a defect, the response from the specimen in through-transmission can give information on wave propagation in the steel. The response at the receiving probe changes with its offset position from the source probe. Because the angle of the backwall reflection must equal the incident *S*-wave angle for a flat surface, changing the probe offset distance gives a different wave propagation path. Using the scanner to position the receiving probe at intervals of offset distances allows precise examination of the changing response.

An offset position of $x = 220$ mm on a 40 mm thick plate gives an angle of propagation of $\theta = 70°$. Fig. 2.12 shows the response at this position. From this time-varying response, often called a trace or A-scan, the pulse arrives at $t \approx 92$ µs. Calculating the expected arrival time of the pulse according to:

$$t_{arr} = \frac{x}{c_s \sin\theta} + t_{wedge} \tag{2.9}$$

using $c_s = 3.2$ mm/µs and $t_{wedge} = 19$ µs we find that $t_{arr} = 92.2$ µs. This agrees with the measured arrival time of the pulse.

The response is "windowed" in time around the arrival of the once-reflected wave path. Within the window smaller amplitude waves arrive at approximately $t = 90$ and 95.5 µs. These waves follow different wave paths than the 1-reflection *S*-wave and arrive at distinctly different times. For example, the *R* surface wave arrives at 90 µs. This wave would not be seen in a smaller time window that ranges from 91–94 µs. Conversely, other waves may arrive before or after the chosen time window and do not appear in this A-

scan. The 3-reflection *S*-wave should arrive at $t = 104$ μs, outside the time window, but cannot be seen in this windowed A-scan.

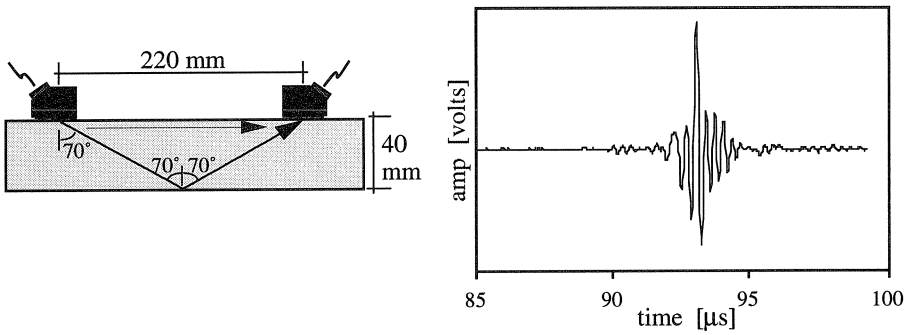

Fig. 2.12. A-scan response [volts] at $x = 220$ mm from 70° probes in through-transmission testing.

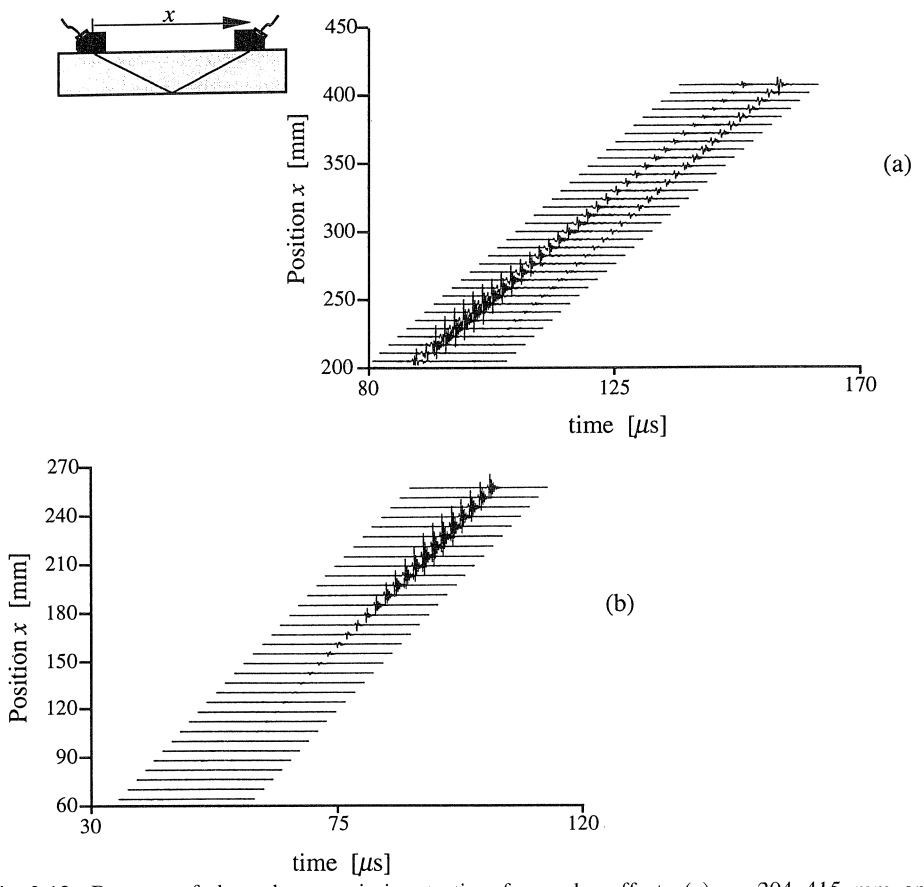

Fig. 2.13. B-scans of through-transmission testing for probe offsets (a) $x = 204$–415 mm and (b) $x = 66$–261 mm.

Changing the position of the receiving probe with the scanner while holding the transmitting probe position constant reveals the change in response of the plate specimen. Fig. 2.13 shows the set of A-scans from offset positions ranging from 66–415 mm. Spatially varying sets of A-scans such as these are commonly called B-scans. Each A-scan is placed on the vertical axis according to its offset position. The vertical scale of the B-scan does not indicate the amplitude of the individual A-scans, however the relative amplitudes of each of the traces are correct.

Fig. 2.13 reveals the advantage of a B-scan in observing waves. The scanned data sets facilitate the identification of the waves and changes in amplitude. The arrival of the 1-reflection wave seems to increase linearly in time. Calculating the slope in the B-scan based on the arrival time in eqn. (2.9) gives

$$\frac{\mathrm{d}x}{\mathrm{d}t} = c_S \sin\theta$$

The slope of the 1-reflection wave in the *B*-scan depends on the angle of propagation. A small angle of wave propagation yields a small slope of the wave in the B-scan. As θ becomes large, the slope of the curve approaches c_S. The propagation angle for a specimen of thickness h is found from

$$\theta = \tan^{-1}\left(\frac{x}{2h}\right)$$

In Fig. 2.13a two separate waves appear within the time window. The angles of propagation represented in the B-scans in Fig. 2.13a ranges from $\theta = 73°$ to $\theta = 79°$. Evident from the relative amplitudes of each of the waves is that while the amplitude of the 1-reflection wave decreases as the offset increases, the amplitude of the second wave increases. The second wave is the beginning of the 3-reflection wave shown in Fig. 2.14.

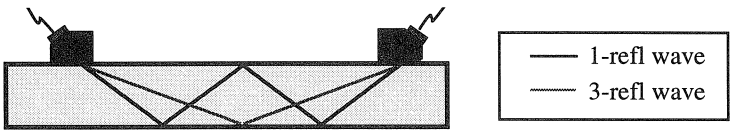

Fig. 2.14. The 1- and 3-reflection wave paths in through-transmission testing.

For through-transmission testing, the expected arrival time and angle of propagation at position x for an n-reflection S-wave are

$$t_{\mathrm{arr-n}} = \frac{x}{c_S \sin\theta} + t_{\mathrm{wedge}} \qquad (2.10)$$

$$\theta = \tan^{-1}\left(\frac{x}{(n+1)h}\right)$$

According to these equations the expected arrival of the 3-reflection *S*-wave at $x = 415$ mm is $t = 157.8$ μs. This calculated time agrees with the arrival time of the 3-reflection wave in Fig. 2.13a. The angle of propagation for the 3-reflection wave ranges from $\theta = 58^\circ$ to $\theta = 69^\circ$ in Fig. 2.13a.

The B-scans in Fig. 2.13, while sufficient for observing arrival times and large changes in amplitude, are inadequate for viewing specific amplitude and duration variation of the waves with offset distance. For this purpose, Fig. 2.15 shows a "focused" B-scan. Shifting each A-scan in Fig. 2.13b in time by the amount $-t_{arr\text{-}1}$ as found from eqn. (2.10) gives the resultant B-scan focused on the 1-reflection wave.

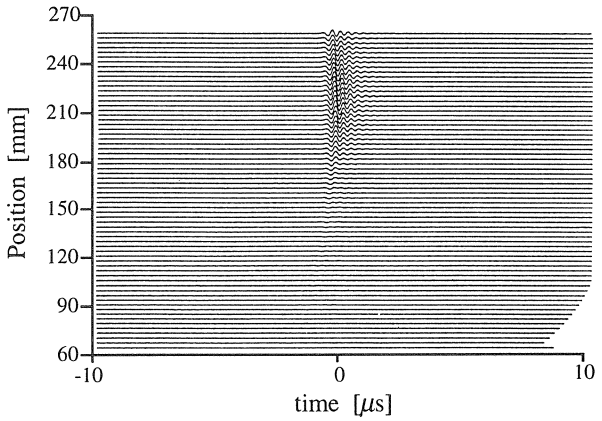

Fig. 2.15. Focused 1-reflection B-scan.

Fig. 2.16 plots the maximum value of each trace in Fig. 2.15 against offset position and angle of propagation. Angle of propagation at each offset position follows from eqn. (2.10) where $n = 1$. The largest amplitude of the B-scan occurs at approximately 70°. At 60° propagation the amplitude decreases by –15 dB. The relative amplitudes of the pulses from each offset position exhibits the directionality of the 70° probe.

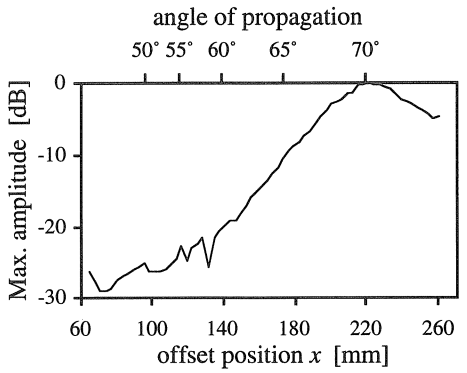

Fig. 2.16. Measured maximum amplitude in trace at offset position x.

Diffraction and scattering attenuation in wave propagation, discussed earlier in this chapter, are sketched in Fig. 2.17. The total amount of attenuation in a wave is determined by the path between the source and receiver. Diffraction attenuation depends on both propagation distance and the angular variation of the receiver from the source probe axis. These types of attenuation are termed axial diffraction and angular diffraction in Fig. 2.17a and 2.17b respectively. Scattering attenuation due to grain boundaries increases with propagation distance. This type of attenuation is termed axial scattering in Fig. 2.17c.

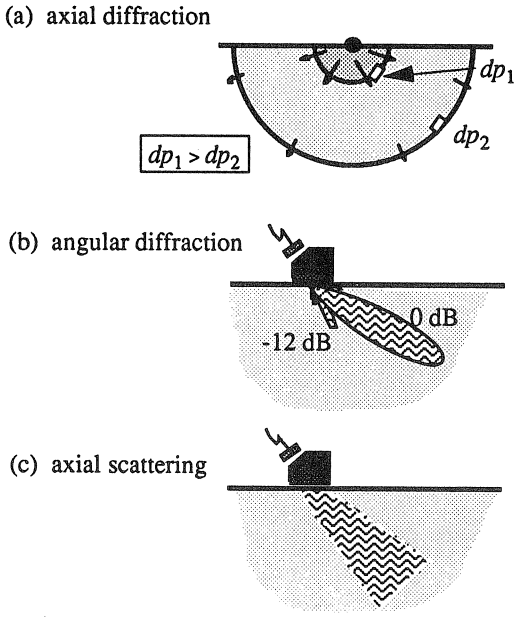

Fig. 2.17. Three forms of attenuation in testing of steel. (a) In axial diffraction the pressure dp decreases as axial distance increases due to spreading of the wave field. (b) Angular diffraction effects of a finite-sized probe cause the pressure to decrease when observed at off-axis angles. (c) Polycrystalline grain boundaries produce scattering attenuation that increases with axial distance from the source.

The scanned measurements can be used to compare and validate the attenuation models. Directionality of the source probe and the scattering during propagation both contribute to attenuation of the wave field. Attenuation from the scattering and diffraction models are shown in Fig. 2.18. Curve (a) shows the attenuation due to scattering at 3 MHz described by eqn. (2.8). The decrease in amplitude due to scattering attenuation A_S when moving from position x_0 to position x_k, on the n-reflection path of a plate specimen of thickness h is

$$A_S = \alpha(l_k - l_0) \tag{2.11}$$

$$l_k = \frac{x}{\sin\theta} = \sqrt{x^2 + [(n+1)h]^2} \qquad (2.12)$$

where l_k and l_0 are the propagation distances when moving from position x_k to x_0. Values of attenuation for scattering are shown in Fig. 2.18a. All the curves in 2.18 are given in [dB] and normalized to the value at $\theta = 70^\circ$.

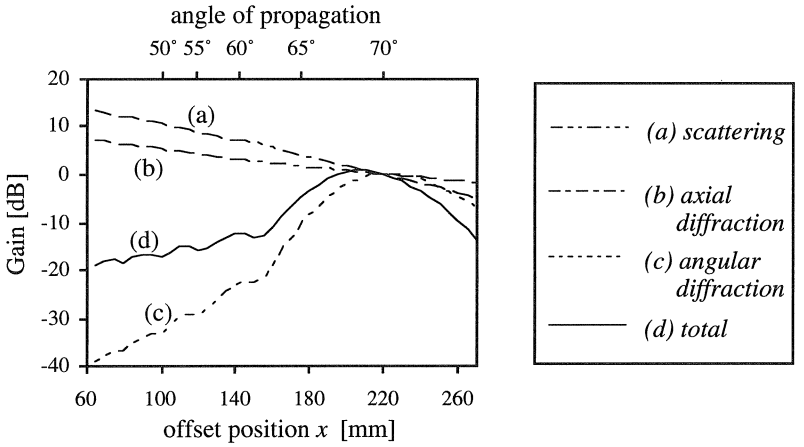

Fig. 2.18. Modeled attenuation due to (a) scattering, (b) axial diffraction, (c) angular diffraction. The total attenuation is shown in (d).

Curve (b) in Fig. 2.18 shows the attenuation due to axial diffraction effects. Scattering effects for Fe 510 steel cause more losses than spreading effects on the axis of the probe. Diffraction effects also cause variations in pressure when the angle of propagation to the receiver deviates from the source axis by θ'. This angular variation constitutes the other component of diffraction. Attenuation due to angular deviation, A_θ, is described by Kinsler, 1962 #3

$$A_\theta = p(r, 0)\frac{J_1(X(\theta'))}{X(\theta')}$$

where $p(r, 0)$ is the on-axis pressure and J_1 is a first order Bessel function. Curve (c) in Fig. 2.18 shows the attenuation due to angular deviation of the offset positions measured with a probe having D = 45 mm. This represents the size of the contact surface on the 70° perspex probe.

Curve (d) in Fig. 2.18 shows the total apparent attenuation resulting from the sum of the three components. The general shape of the total attenuation curve depends on angular diffraction behavior. Attenuation due to axial diffraction contributes very little with respect to the attenuation from angular diffraction. Scattering attenuation, while the only factor in determining the peak frequency of the response, is still not as important as

angular diffraction attenuation in determining the amplitude of the response. Of the three contributors to attenuation, scattering is the only component that has been derived from empirical values from measurements. The axial and angular diffraction curves are based on theory of a piston radiator.

Fig. 2.19 shows a comparison of the expected amplitude profile from the attenuation models and the measured amplitude profile from scanning. The modeled curve is repeated from Fig. 2.18d. Measured data points come from Fig. 2.16. The maximum value of each of the curves in this figure are normalized to 0 dB at 70°.

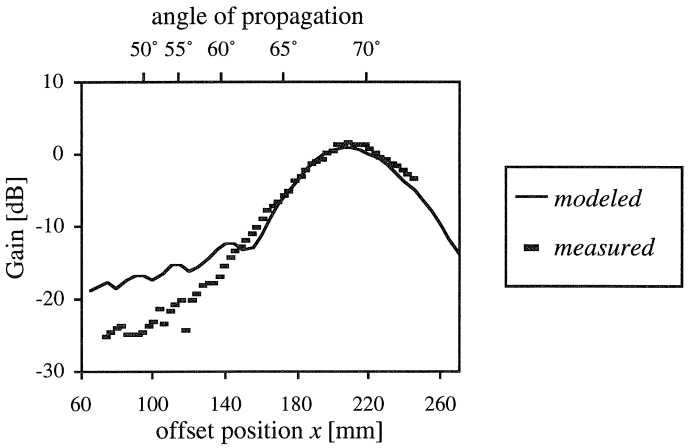

Fig. 2.19. Modeled and measured normalized amplitude profiles of B-scan traces.

Within the range of 65°–75° the modeled attenuation curve shows excellent agreement with measured amplitudes. At propagation angles lower than 60° measured amplitudes are lower than expected. Errors at these large angular deviations most likely result from the receiving probe orientation. The receiving probe converts an *S*-wave to a *P*-wave in exactly the opposite sequence as shown for the send probe in Fig. 2.3. Mode conversion at the interface and the orientation of the transducer are optimized for incoming and outgoing 70° *S*-waves. The angular-dependent receiving sensitivity of the probe is the same as its sending directivity pattern. (Krautkrämer, Krautkrämer 1990) At large deviations from the axis of the probe smaller amplitude waves are sent as well as received. Therefore, the probe will not transfer the full surface response of a 50° incoming *S*-wave as it would a 70° S-wave.

2.4 *Defect detection*

A defect located within an ultrasonic wave field constitutes a potential source of scattering in the field. The defect provides both a surface for reflection and possibly a tip for diffraction. Directionality of the scatterer depends upon the nature and orientation of the defect. Certain limitations are placed on the defects considered in this work to facilitate their measurement and analysis.

Only planar defects are considered in testing because of their highly-directional reflected field. Although non-planar defects can be detected with ultrasonic testing, at large distances their reflected energy is too diffuse to measure. The response from a non-planar defect may spread considerably. This results in small levels of energy at large distances. A further constraint on the synthetic defect considered in testing is that its plane is limited to perpendicular orientation relative to the axis of testing. This allows a linear probe configuration as well as a 2-dimensional analysis of the wave field as shown in Fig. 2.20a. An off-axis orientation of the defect, shown in Fig. 2.20b, requires a more complex analysis of the wave paths. Finally, the plane of the defect is normal to the surfaces of the plate specimen, as seen in the side view of Fig. 2.20a. This limitation quite accurately characterizes fatigue-induced cracks. In addition, assuming a smooth defect surface, normal orientation greatly simplifies modeling of the paths.

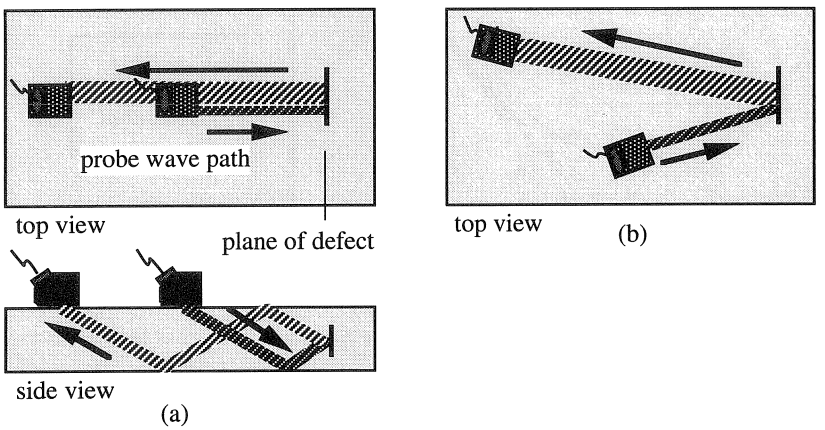

Fig. 2.20. Position of planar defect relative to probes (a) on-axis orientation and (b) off-axis orientation.

All defects considered in testing are initiated with electron discharge machining (EDM) notches. EDM notches feature relatively sharp tips compared to mechanical machining and can have surfaces that simulate the roughness of a fatigue crack.
Fatigue cracks and fabrication errors generally arise in the vicinity of welds. As a result, all surface-breaking defects generated are located at the toe of a welded connection. Bending or scattering of waves through the weld material in the specimens is not observed in measurements. (Chinn 1990)

2.4.1 Measurement configurations

Three measurement configurations using angled probes exist for defect detection in steel. Time-of-flight, pulse-echo and pitch-catch setups all use surface probes to send an angled wave in the direction of a defect. Fig. 2.21 shows the three configurations.
Time-of-flight measurements observe the diffracted field from the defect tip. The diffracted energy from a sharp tip is distributed over a wide range of angles as seen in Fig. 2.22a. Given the wave speed in the specimen and the location of the probes, the

arrival time or "time-of-flight" of the diffracted wave indicates the location of the defect tip. This technique is very effective in localized testing. (Terpstra et al. 1989) (Ravenscroft et al. 1991) However, accessibility requirements described in Chapter 1 preclude the use of probes on both sides of the defect. Further, because of the wide distribution of energy in the diffracted field this technique requires close proximity of the probes to the defect, rendering it inapplicable to long-distance testing.

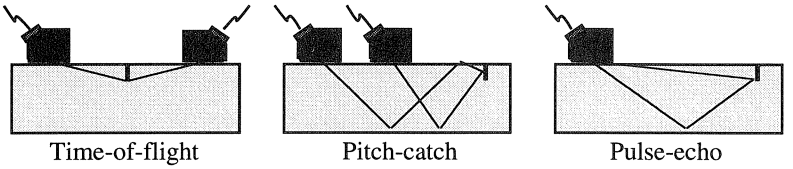

Fig. 2.21. Time-of-flight, pitch-catch and pulse-echo test configurations for defect detection.

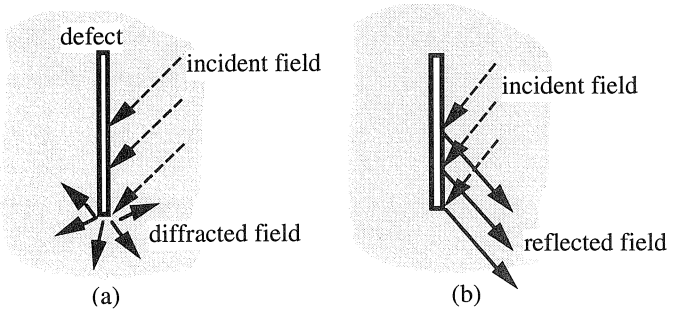

Fig. 2.22. Scattered energy from a notch or defect has two parts, (a) the diffracted field and (b) reflected field.

Pitch-catch testing uses two probes on the same side of the defect. One probe transmits the illuminating wave field, the other receives the scattered field from the defect. Both the reflected (Fig. 2.22b) and diffracted fields contribute to the response in pitch-catch testing. The relative magnitudes of the reflected and diffracted fields depend primarily on the character of the defect. Defects with rough surfaces and a very sharp tip produce more diffracted energy. Conversely, if the defect has smooth surfaces relative to the wavelength of testing, the reflected energy is much larger than the diffracted energy. Fatigue cracks and EDM notches fall into the latter category of defects. (Chinn, Dieterman 1991) Although the tips are sharp, the surfaces of the cracks are relatively smooth producing a large reflected field that dominates the diffracted field. Only the reflected field is discernible on the illuminated side of the defect. The diffracted field is too small to discern in the presence of the reflected field.

Pulse-echo testing uses one probe to both transmit and receive. A single probe test setup is more versatile than dual probes allowing greater accessibility to testing areas. As in pitch-catch testing, the sender and receiver are on the same side of the defect. The reflected energy from a normally-oriented fatigue crack subject to pulse-echo testing is much larger than the diffracted energy. (Chinn, Dieterman 1991) In pulse-echo testing of

oblique defects however, the orientation of the defect relative to the incident wave is another factor in the relative magnitudes of measured diffraction and reflection fields.
If the plane of the defect is oblique relative to the plate surfaces the measured response may be dominated by the diffracted field. This is also true in pitch-catch testing however the receiver position can be adjusted to take advantage of the larger reflected field. Fig. 2.23a shows an oblique defect in pitch-catch testing. The reflected wave propagates to the receiving probe, overwhelming the diffracted field (shown with the dotted line). For most defect orientations, the response at the receiving probe is almost always dominated by the reflected field. Pulse-echo testing of an oblique defect, shown in Fig. 2.23b, can only measure diffracted responses for some orientations. The reflected field misses the coupled transmit/receive probe for the orientation shown. Because only normally-oriented planar defects are considered in this work, it is assumed that the reflected field dominates scattering in both pulse-echo and pitch-catch testing.

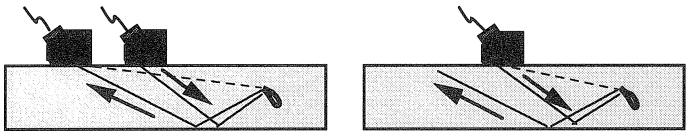

Fig. 2.23. Reflected and diffracted (dotted line) paths of an obliquely-oriented defect in (a) pitch-catch testing and (b) pulse-echo testing.

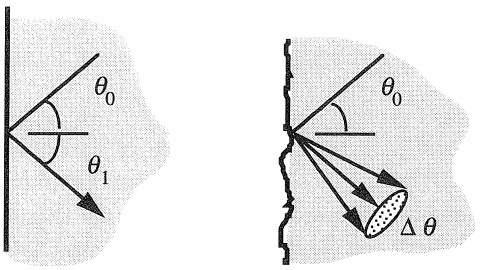

Fig. 2.24. *S*-wave reflection from a free surface (a) smooth, specularly-reflecting surface (b) rough, scattering surface.

Separate transmitting and receiving probes in pitch-catch testing of fatigue cracks also have the advantage of measuring a stronger response than with pulse-echo testing. An *S*-wave incident on a perfectly smooth, free surface reflects at an angle θ_1 as shown in Fig. 2.24a. Reflection from this type of surface is termed specular reflection. If the surface is rough relative to the wavelength of propagation (Fig. 2.24b), scattering occurs upon reflection. The extent of scattering is dependent on the surface roughness. (Ogilvy 1988) Rough surfaces with wide height distributions produce large amounts of scattering yielding a large $\Delta\theta$ around the specular angle of reflection.

Pulse-echo testing, with its single probe, relies on scattering at the defect to obtain a response. Fig. 2.21 shows a pitch-catch configuration, measuring the specular response

from a defect, and a pulse-echo configuration, measuring the scattered response. Because of the single probe in pulse-echo testing, the response must be measured from a non-specular path. Only a separate transmitter and receiver allow measurement of the specular reflection. Illuminated defects with surface roughness much smaller than the wavelength of the incident wave, such as fatigue cracks, reflect most of their energy specularly. Scattering energy is lower but always present because the surface of the fatigue crack is never completely smooth. Pitch-catch configurations primarily measure specular reflections and therefore produce stronger responses from fatigue cracks than pulse-echo configurations.

2.4.2 Defect detection of surface defects

Ultrasonic testing is capable of detecting both surface and embedded defects. Surface-breaking defects are the most common type found in practice. When compared to embedded defects, surface defects present more immediate danger because they are usually located at the point of highest stress within the thickness. This section discusses detection and observation of surface defects under cyclic loading.

2.4.2.1 Scanning measurements

Scanning configurations of a 40 mm steel plate specimen are shown in Fig. 2.25. In pitch-catch testing the transmitting 70° *S*-wave probe illuminates the defect area from an offset position of 165 mm. This transmitting position is fixed while the receiver scans a range of positions. At a transmitting position of 165 mm, a 70° wave illuminates a point halfway through the thickness at the defect after 1-reflection. Other points through the thickness are illuminated with larger or smaller angles of incidence. The receiving probe is scanned between 290 mm–900 mm offsets from the defect at 3 mm intervals. Pulse-echo testing of the same plate specimen uses a single 70° *S*-wave probe scanning from 165 mm–920 mm.

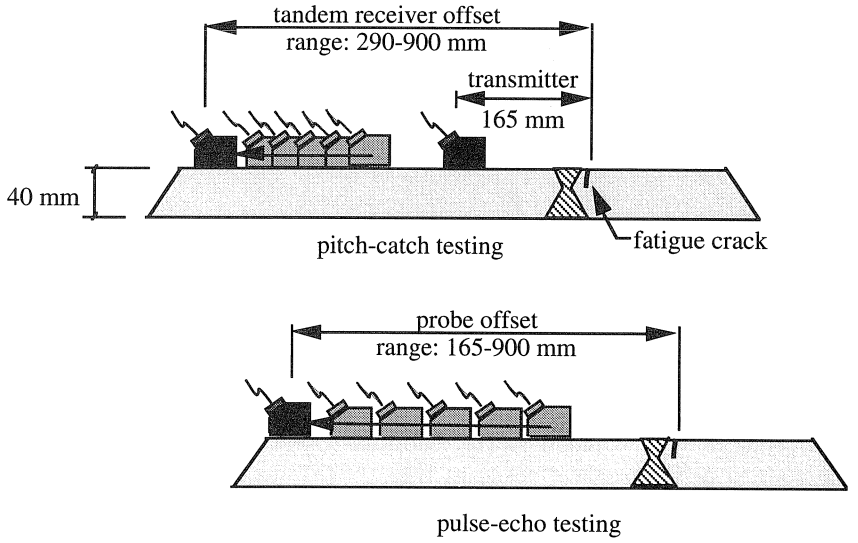

Fig. 2.25. Pitch-catch and pulse-echo scan test configurations.

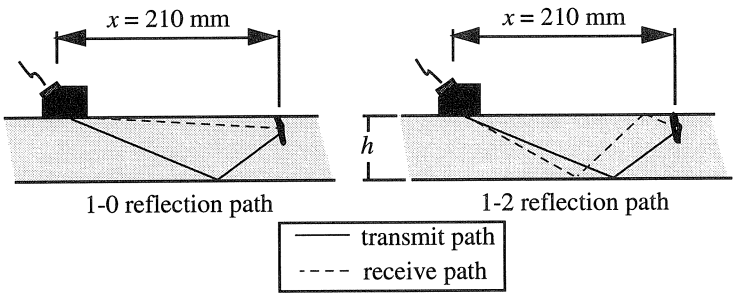

Fig. 2.26. Two possible pulse-echo paths from offset position x = 210 mm.

Two pulse-echo reflection paths, the 1–0 path and the 1–2 path, at an offset position 210 mm from the defect are shown in Fig. 2.26. The 1-0 path has 1 reflection to the defect and 0 plate surface reflections on the return path. A 0–1 path, with the transmit and reflected paths reversed from the 1–0 path, has exactly the same path length as the 1–0 path. The 1–0 and 0-1 paths arrive at the same time and are indistinguishable in the time domain. Henceforth an *n-m* path in pulse-echo testing denotes both the *n-m* and *m-n* paths.

The 1-2 path uses the same path to the defect as the 1–0 path but returns on a path that has 2 plate surface reflections. The 1–0 and 1–2 paths use different scattered paths from the defect surface in order to return to the same probe location. The number of measurable reflection paths from a defect is determined by the probe directionality together with the extent of scattering at the defect. Pulse-echo scanning in the offset range 165 mm–370 mm of a surface-breaking defect with a depth and length of 10 mm and 29 mm, respectively, produces the B-scan in Fig. 2.27a. Separate waves from several different paths are discernible within the time window. The arrival time of the *m-n* wave resulting from pulse-echo testing at offset position x is

$$t_{\text{arr m–n}} = t_{\text{wedge}} + \frac{1}{c_S}\left\{\sqrt{[(m+1)h + \varepsilon_m y]^2 + x^2} + \sqrt{[(n+1)h + \varepsilon_n y]^2 + x^2}\right\} \tag{2.13}$$

where

ε_m, ε_n = +1 for even m and n, respectively,
ε_m, ε_n = –1 for odd m and n, respectively

and h is the plate thickness. Shifting each trace in the B-scan by the arrival time of the 1–0 wave reflecting from y = 2 mm at the crack location allows identification of the wave and its amplitude at different offset positions (Fig. 2.27b). Focusing on the 1–2 reflection (Fig. 2.27c) shows that the 1-2 path in this offset range has higher amplitudes than the 1-0 wave. Illumination and reflected energy in the 1-2 path combine to produce a higher

response at these offsets. The other two paths in the shifted B-scans are identified using focusing as the 0–3 and 2–3 / 1-4 paths. The 1–4 path has almost the same arrival time as the 2–3 path in pulse-echo testing and cannot be separated from it.

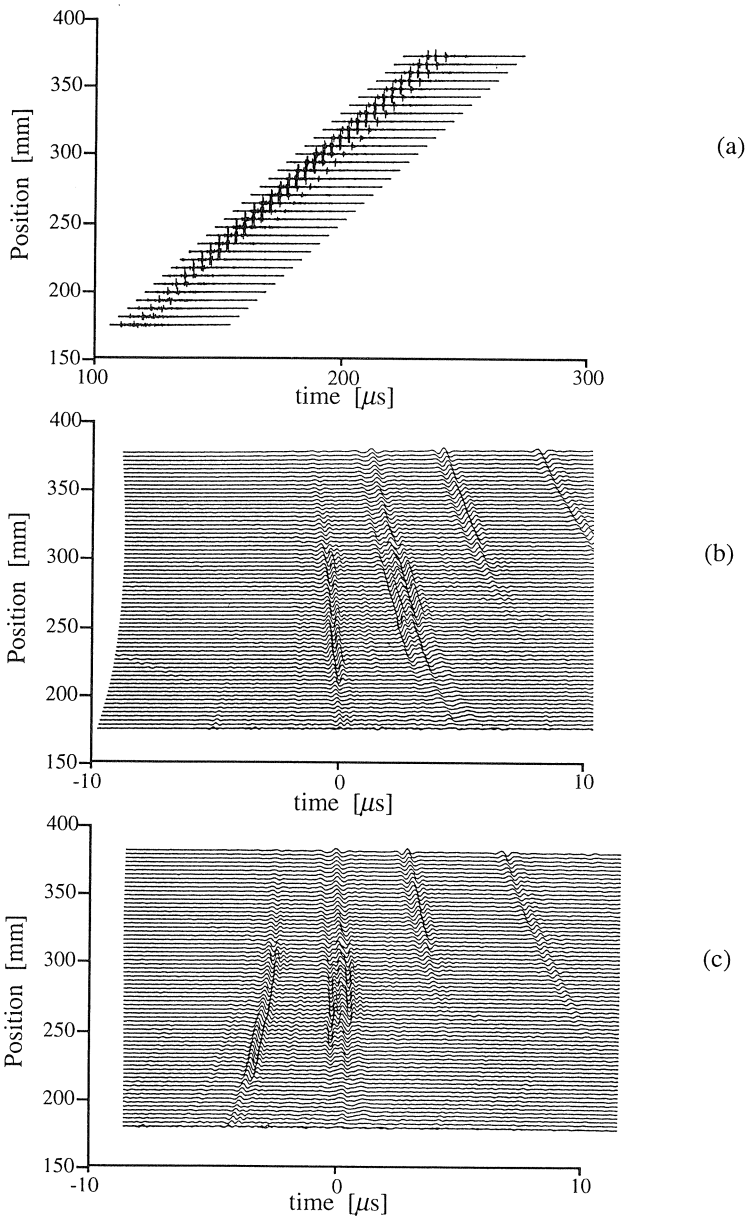

Fig. 2.27. Pulse-echo data for probe offset range 165 mm to 370 mm from a surface defect with depth 10 mm. (a) B-scan data, (b) B-scan focused on 1-0 reflection, (c) B-scan focused on 1–2 reflection.

In the offset range 780 mm–920 mm, pulse-echo wave paths are still discernible for the 10 mm defect. Fig. 2.28 shows the pulse-echo B-scan and the shifted B-scan for the 5–6 reflection path from this range. Even at these large distances the shifting equation (eqn. (2.13)) effectively predicts the arrival time of the 5–6 path. Although the signal-to-noise ratio is much lower than with closer ranges of testing, shifting the traces according to the path arrival time helps identify the wave. At approximately –8 μs in Fig. 2.28b the 4–5 reflected path occurs and appears almost in focus. Similarly, the 5–8 reflection path occurs at approximately +8 μs and also has sufficient energy to be detected. Detection of the 10 mm × 29 mm (depth × length) defect on a 40 mm plate from long distances is clearly possible with pulse-echo testing.

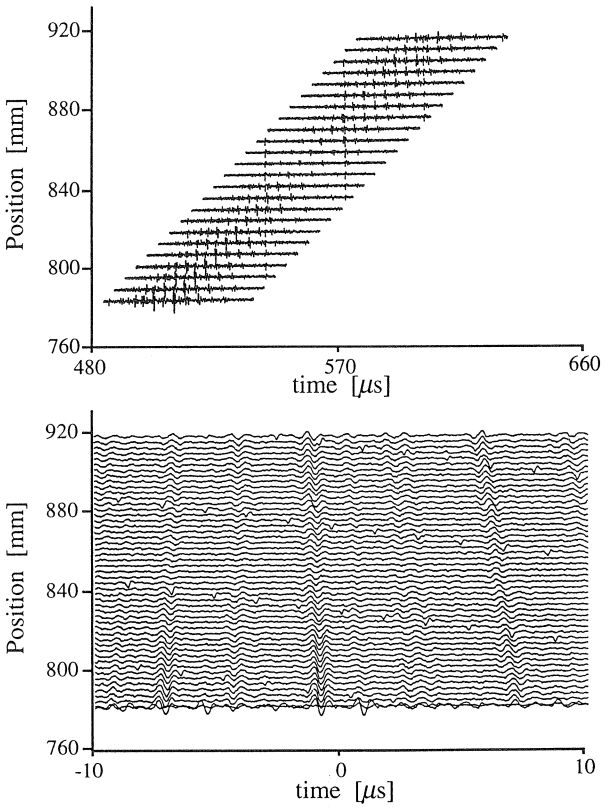

Fig. 2.28. Pulse-echo testing in the range 780 mm–920 mm (a) B-scan from a 10 mm deep surface defect (b) Shifted B-scan for the 5–6 reflection path.

Pitch-catch testing configurations can also detect the 10 mm × 29 mm defect from long-distances. The decoupled transmitter and receiver featured in pitch-catch testing allow more wave paths at each offset. Fig. 2.29a presents the B-scan from pitch-catch testing of the 10 mm defect with the configuration in Fig. 2.25. In this B-scan the receiver offset ranges from 700 mm–900 mm. More paths are visible in each pitch-catch testing trace than in Fig. 2.28a for pulse-echo testing. The arrival time for the *m-n* path using a pitch-

catch testing configuration with the transmitting probe located at $x_{transmit}$ and the receiving probe at $x_{receive}$ is

$$t_{arr\ m-n} = t_{wedge} + \frac{1}{c_S}\left\{\sqrt{[(m+1)h + \varepsilon_m y]^2 + x_{transmit}^2} + \sqrt{[(n+1)h + \varepsilon_n y]^2 + x_{receive}^2}\right\} \tag{2.14}$$

Figs. 2.29b-c show the B-scan shifted in time for the 1–6 and 1–8 reflections. Pitch-catch testing gives a better signal-to-noise ratio than pulse-echo testing at these offsets. Positioned at 165 mm from the defect, the transmitting probe illuminates the defect area from a relatively close distance. In pulse-echo testing the transmitting offset is the same as the receiving offset resulting in a longer path length and less energy in the returned signal. Both the 1–8 and 1–10 paths have strong responses in this offset range. The path arriving between these paths is identified as the 0–7 path. The 0–7 path has an equally strong response as the 1–8 and 1–10 paths. All 3 of the paths appear to have their largest response in this offset range. Pitch-catch testing, like pulse-echo testing, can detect a 10×29 mm defect from long distances.

2.4.2.2 Crack growth observation

At intervals of crack growth the plate specimen is unloaded and tested using pulse-echo and pitch-catch testing. Because the exact depth and shape of the crack are unknown during loading, intervals are chosen based on the crack length. The crack shape is marked by decreasing the load for 40 kcycles between testing intervals. Delineation by the marks reveals the precise shape of the crack upon breaking of the plate. Increasing in length as well as depth, the shape of the crack remains semi-elliptical throughout loading.

Comparison of the pulse-echo response from offset distances $x = 210$ mm and $x = 920$ mm are shown in Fig. 2.30 for crack surface area. The crack surface area is calculated from a half-ellipse given the length and depth of the crack. At the closer probe position of $x = 210$ mm the response is on average +20 dB higher than when the probe is positioned at $x = 920$ mm for all crack sizes. Longer propagation distances allow the wave to attenuate more. As the crack grows, the amplitude of the response generally increases. Between the individual measurements there appears to be a certain amount of error or uncertainty in the increase. This may result from measurement error or from the changing crack surface morphology.

The response from pitch-catch testing of a growing crack is shown in Fig. 2.31 for receiver positions $x = 300$ mm and $x = 900$ mm. As in pulse-echo testing, the response at the closer receiver position is on average +20 dB higher than the farther offset. Responses from pitch-catch testing increase with crack size as expected. There seems to be less uncertainty in the increase between individual measurements than with pulse-echo testing.

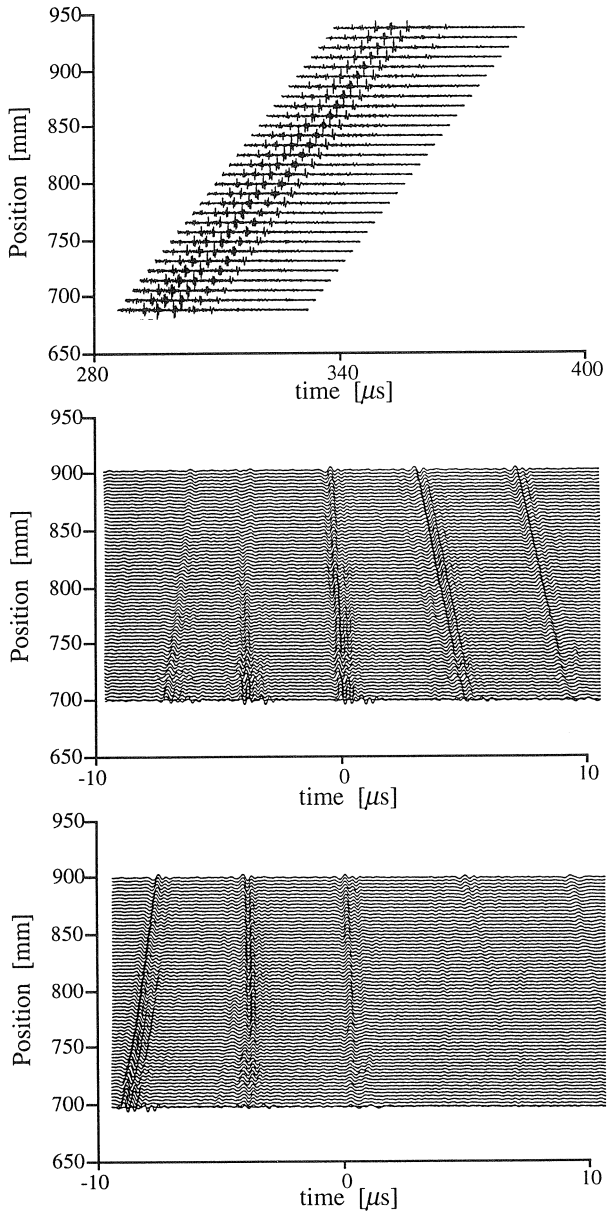

Fig. 2.29. Pitch-catch configuration data for receiver offset range 700 mm–900 mm testing a 10×29 mm defect. (a) B-scan data (b) B-scan focused on the 1–6 reflection path (c) B-scan focused on the 1–8 reflection path.

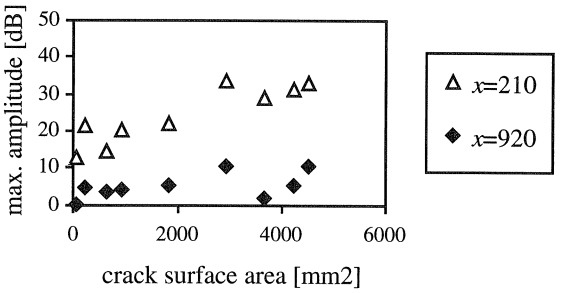

Fig. 2.30. Pulse-echo response from offset positions $x = 210$ mm and $x = 920$ mm for increasing crack size.

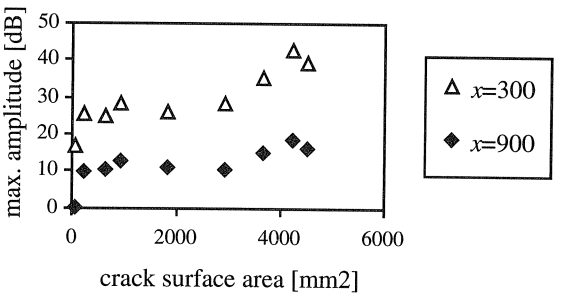

Fig. 2.31. Pitch-catch testing response from receiver offset positions $x = 300$ mm and $x = 900$ mm for increasing crack size.

Both pulse-echo and pitch-catch testing methods are sensitive enough to measure changes in crack size from distances of 900 mm from the defect. Pitch-catch testing has more consistent measurements than pulse-echo testing. This consistency most likely results from the decoupled transmitter and receiver that provides a strong illumination field for pitch-catch measurements. More paths are available in a given range with pitch-catch testing. Pulse-echo testing, relying exclusively on non-specular reflected paths, is more susceptible to changes in the crack surface as it grows. Pitch-catch testing obtains large responses from the specular reflection. The specular response may vary with crack growth, however, because the plane of the crack remains normal to the plate surfaces, the strongest response remains specular for most reasonable surface roughnesses.

3 Processing techniques

3.1 *Synthetic aperture focusing technique*

Focusing techniques demonstrated in Chapter 2 allow easier identification of wave paths when considering B-scan data sets. Shifting each trace in time focuses the scan data set on the response from a single point in the medium. The travel time to and from the point in focus determines the time shift at each offset position.

Some ultrasonic testing applications use focused probes to achieve higher sensitivity to defects than conventional probes. (Krautkrämer, Krautkrämer 1990) Focused probes contain concave transducers that focus on a specific point in a solid with very little spreading of the wave field. The presence of a reflector at the focus point returns a very strong signal with most of the input energy (Fig. 3.1a). While appropriate for some specific applications, these types of transducers are not flexible enough for use in general detection. However, processing scanned data can simulate the qualities of a focused transducer. The time-shifting technique in Chapter 2 effectively uses the response at successive point sources to simulate a focused probe.

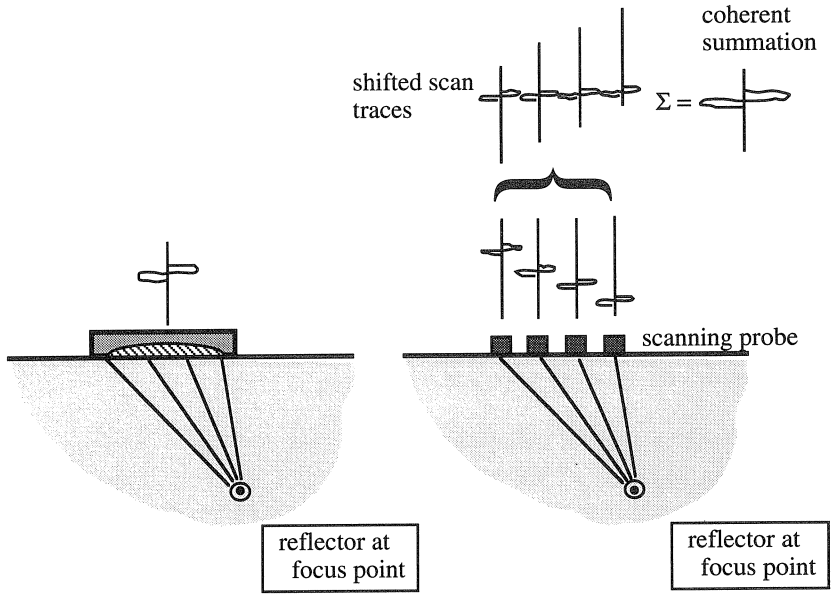

Fig. 3.1. Focusing on a point in the medium in the presence of a reflector: (a) using a focused probe, (b) by shifting scanned data.

Processing scan data can simulate a large focused probe whose diameter is the length of the scan. Fig. 3.1b shows traces from scanned data shifted in time, focusing on the selected point. Summation of the focused traces gives a coherent signal equivalent to that found with a focused probe. A reflector close to, but not at the focus point produces a smaller response from the synthesized probe just as with a focused probe. The summation of the focused traces indicates the presence of a reflector as shown in Fig. 3.2b that is weaker and more diffused than if the reflector were at the focus point as in Fig. 3.2a. When no reflector occurs in the vicinity of the focus point zero response results as shown in Fig. 3.2c.

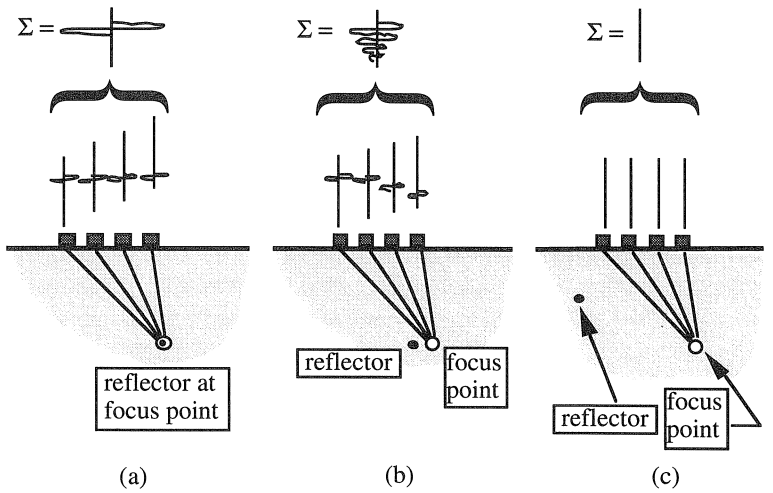

Fig. 3.2. Summation of focused signals with (a) a reflector present at the focus point, (b) the reflector close to the focus point, (c) no reflector in the vicinity of the focus point.

Shifting the traces effectively finds the coincident point or points among the possible reflector locations from each trace. Fig. 3.3a shows the set of possible reflector points in the medium that can result in a response at $t_1 = 2l_1/c$. The set of all possible reflector points form a semicircle with equivalent travel times at distance l_1. The response from two measurement points reduces the possible locations of the reflector to the coincident points of the respective equidistant semicircles as in Fig. 3.3b. Many coincident points result for measurement points within close proximity of one another. Increasing the range covered by the set of measurement points decreases the set of coincident points. The size of the actual reflector bounds the lower limit of the set of coincident points.

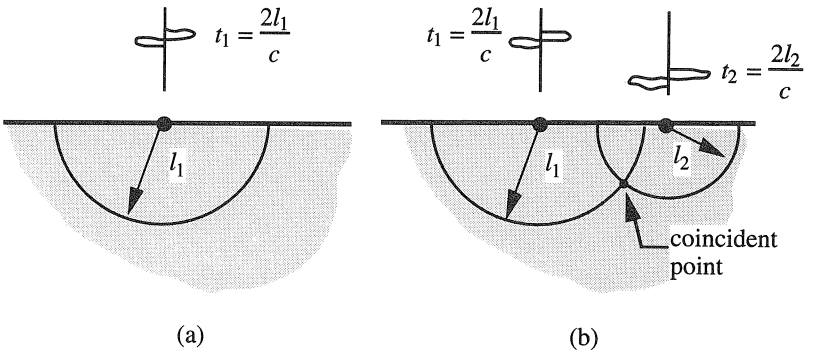

Fig. 3.3. Possible reflector locations in free-field propagation form a semicircle (a) equidistant points resulting from measurement from a single point, (b) measurements from two points reduces the possible reflector locations to the coincident points.

In non-destructive testing, this focusing and summation procedure is called the synthetic aperture focusing technique (SAFT). (Doctor et al. 1986; Seydel 1982) SAFT performs

spatial characterization of a solid from ultrasonic testing measurements. Using pulse-echo or pitch-catch data, SAFT identifies reflections and wave paths resulting from a defect in a solid. When focused, these reflected paths provide information on the location and nature of the defect. SAFT-imaging uses the reflected paths to construct an image of the defect. Images produced by SAFT-processing of data indicate points of reflection or scattering in the area of interest.

3.1.1 SAFT-imaging from pulse-echo measurements

SAFT-imaging provides a visual image of an area in the solid. Fig. 3.4 shows the process of SAFT-imaging on a plate specimen scanned with a pulse-echo probe. A grid divides the area of interest into a set of points with spacing smaller than the wavelength of testing, λ. This prevents undersampling of responses in the image. Each point in the grid has a characteristic travel time function with respect to the offsets, x, of the scanned range for a given wave path. Fig. 3.4 shows two travel time functions corresponding to the offsets in the scanned positions relative to points A and B in the grid. The travel time functions assume the same m–n wave paths between the offset positions and the mesh points.

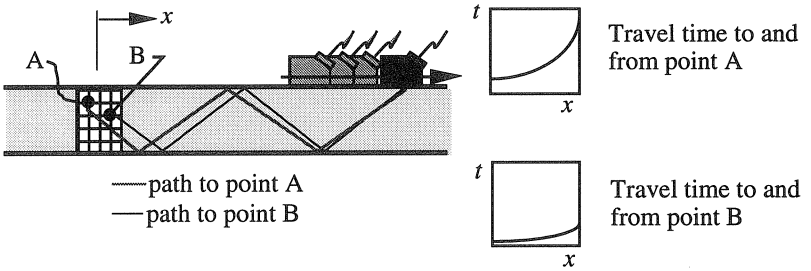

Fig. 3.4. SAFT-imaging of an inspected region of a plate.

Obtaining an image entails successively focusing the scan data set on each point in the grid. The coherent summation of the shifted traces at the expected arrival time from point A becomes associated with mesh point A. The summation of shifted traces at point B corresponds to mesh point B. Repeating the process for all the other points supplies a coherent sum for each grid point. The collection of these coherent sums into a grid produces a SAFT image . When no reflector occurs at the focus point in the test specimen a small coherent sum at that SAFT grid point results. The presence of a reflector at the focus point in the specimen results in a large sum.

In Chapter 2, Fig. 2.27a shows traces from the pulse-echo configuration in Fig. 2.25 testing a 10 mm deep surface-breaking fatigue crack. The travel time of the 1–0 wave path between the probe and a focus point 2 mm from the surface at the crack location increases with probe position according to eqn. (2.13). This is the travel time function for the pulse-echo scan. Shifting each trace in the scan by its travel time to and from the focus point results in the focused data set in Fig. 2.27b.

SAFT images of the crack area, derived from the data in Fig. 2.27a, are shown in Fig. 3.5. The SAFT images contain a 128 × 128 point grid representing a 15 mm × 40 mm area of

interest centered at the crack location as indicated in Fig. 3.5a. Fig. 3.5b shows the size and location of the actual fatigue crack relative to the SAFT image size. The SAFT grey-scale images in Fig. 3.5c and d show dark areas to indicate grid points with large summation values and light areas to indicate points with small summation values. Fig. 3.5c shows the SAFT image found using the 1–0 reflection path to focus on each point in the grid. Fig. 3.5d uses the 1–2 reflection path to focus on grid points.

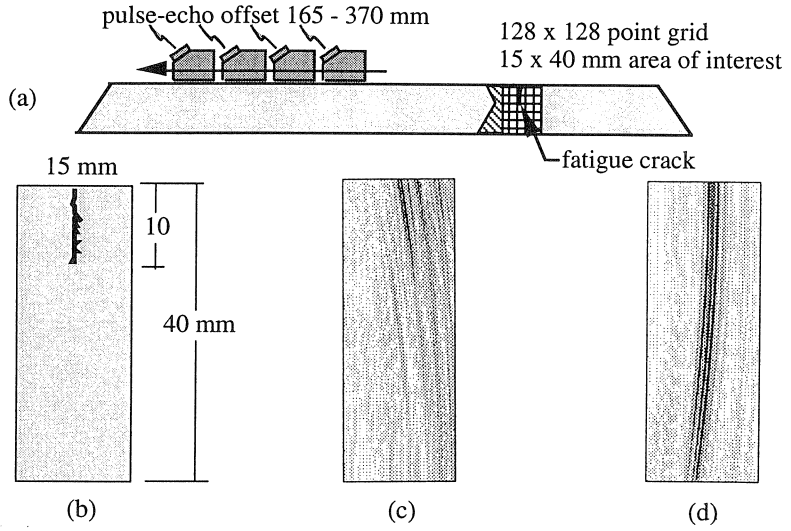

Fig. 3.5. SAFT images of a 10 mm fatigue crack using pulse-echo testing in the offset range 165 mm–370 mm, (a) Measurement configuration and location of area of interest in SAFT images. (b) actual location of fatigue crack in image area (c) SAFT image from 1–0 mm reflection path (d) SAFT image from 1–2 reflection path.

Both images in Fig. 3.5c and d locate the crack at the correct offset position on the plate. However, resolution of the actual crack size is not possible from either of the images. The SAFT image in Fig. 3.5c gives better resolution of the 10 mm fatigue crack than the image in Fig. 3.5d. The indication in the 1–0 reflection image extends to the upper third of the plate, correctly estimating the depth of the actual crack. The 1–2 reflection SAFT image in Fig. 3.5d has an indication that erroneously represents the actual depth of the crack. It shows a defect extending to the full depth of the cross-section. Both images use the same measured data set however different focusing paths generate different images. Comparison of the two images shows that characterization accuracy decreases with path length and configuration.

The accuracy of defect characterization using pulse-echo testing depends on the path length to the imaging area relative to the aperture size. For a given synthetic aperture size, longer path lengths decrease the characterization ability of the SAFT image. The set of indications in the SAFT image includes the actual defect surface. A large aperture relative to the path length limits the set of indications to those points on the defect surface. As the aperture-path length ratio becomes smaller, resolution decreases and other indications

appear in the SAFT image. False indications arise at points on the SAFT grid whose travel times equal the travel time to the real reflector.

High frequency wave propagation in a flat plate undergoes multiple reflections from plate surfaces. Multiple reflections can be idealized with free-field wave propagation traveling through layers. Fig. 3.6 shows the idealized pulse-echo 1–2 reflection path resulting from a defect. The propagation path to the defect, l_1, reflects once before reaching the defect and therefore passes through one layer before reaching the defect. The path from the defect, l_2, reflects twice before arriving at the receiving probe and therefore passes through two layers. Each pass through a layer boundary represents the reflection of the wave from the actual plate surface. *S*-waves incident upon a plate surface reflect an *S*-wave at an angle equal to the incident angle, as given by Snell's law. When traveling across the idealized layer boundary, the wave effectively reflects at its incident angle. Reflection from the defect occurs in the illuminated layer.

The set of points with the same total propagation distance, $l_1 + l_2$, form an ellipse whose major axis lies on a line between the probes. These points also have the same travel time, given by $(l_1 + l_2) / c$. By definition, the equidistant ellipse has length $(l_1 + l_2)$. The foci of the ellipse coincide with the probe positions.

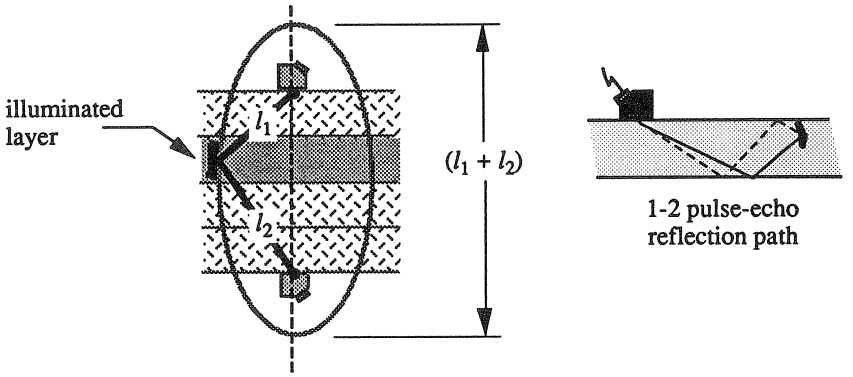

Fig. 3.6. Layer idealization of a pulse-echo 1–2 reflection path.

The SAFT image in Fig. 3.5c uses the response from the travel time of the 1–2 path to determine the coherent sum at the grid position. A large response measured at that time point can be attributed to a reflector at any point along the ellipse within the illuminated layer and in the direction of the probe axis. Marked with a thicker line in Fig. 3.6, these points have equivalent travel times and equidistant propagation paths.

Coherent summation of the responses from a large aperture eliminates some of the equidistant points in the illuminated layer, depending on the size of the aperture. Fig. 3.7 shows ellipses of equidistant length from several pulse-echo offset positions. The coherent sum of responses in the aperture limits indications in the SAFT image to coincident points on the ellipses. The 1–0 reflection path shown in Fig. 3.7a has a large aperture relative to the propagation distance. Coincident points of the ellipses from each offset position are limited to a small area of the illuminated layer. In Fig. 3.7b the 1–2 path has

a longer total propagation distance and the same size aperture as in Fig. 3.7a. More coincident points occur in the illuminated layer than in the 1–0 reflection path. This explains the erroneous characterization of the crack in the SAFT image in Fig. 3.5c and the elliptical curve of the indication. Good characterization requires a large aperture relative to the length of the wave path.

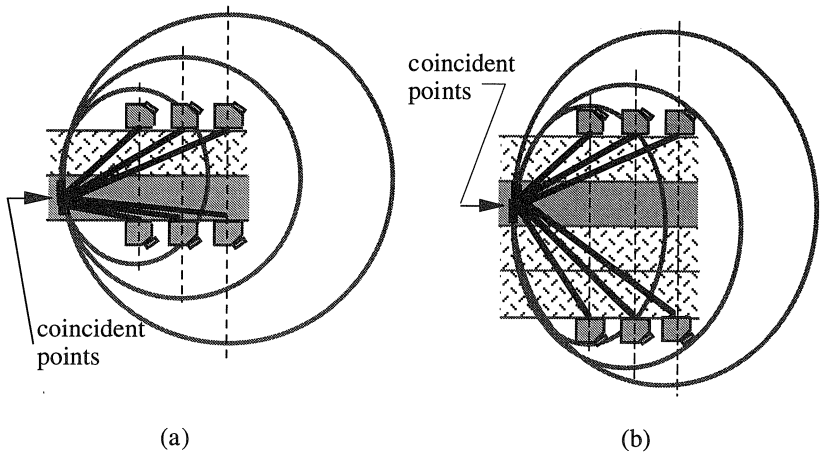

Fig. 3.7. Ellipses of equidistant path lengths for increasing pulse-echo offset positions. SAFT image indications are limited to the coincident parts of the ellipses. (a) 1–0 reflection path, (b) 1–2 reflection path.

Sensitivity studies in (Johnson 1982) show that the optimum synthetic aperture size for good resolution of a defect equals the beam width of the probe at γ_{-20dB} as shown in Fig. 3.8. Good resolution requires a synthetic aperture, $D_{synthetic}$, larger than the –20 dB beam width at propagation distance L, indicated in Fig. 3.8 by B_{-20dB}. Finding the optimum $D_{synthetic}$ for a given ray path entails determining the –20 dB beam width at the propagation distance L of the ray path. Smaller synthetic apertures result in exaggerated SAFT image indications. Because the probe beam width increases linearly in the farfield, the optimum synthetic aperture size increases linearly with propagation distance. The images in Fig. 3.5 confirm that resolution decreases with propagation length. The optimum synthetic aperture on the plate surface for the 1–2 pulse-echo path using the 70° probe is 260 mm. False indications in Fig. 3.5b result from the smaller 205 mm synthetic aperture size used to generate the image.

Pulse-echo testing from long distances requires a large aperture. Scanning over such a large aperture may not always be possible. Despite the oversized indication of the defect in the SAFT image of Fig. 3.5c, detection and lateral location capabilities remain very good. Fig. 3.9 shows the effect of increasing the testing distance on a SAFT image while maintaining a 200 mm aperture. A 10 mm deep surface-breaking fatigue crack on a 40 mm thick plate is tested in pulse-echo from 90 mm–970 mm offset distance. The SAFT image of a 15 mm × 40 mm section of the plate at the location of the crack comprises a 100 × 100 point grid centered about the crack. All images have a synthesized

aperture of 200 mm. Each image uses the wave path with the highest response in the testing range.

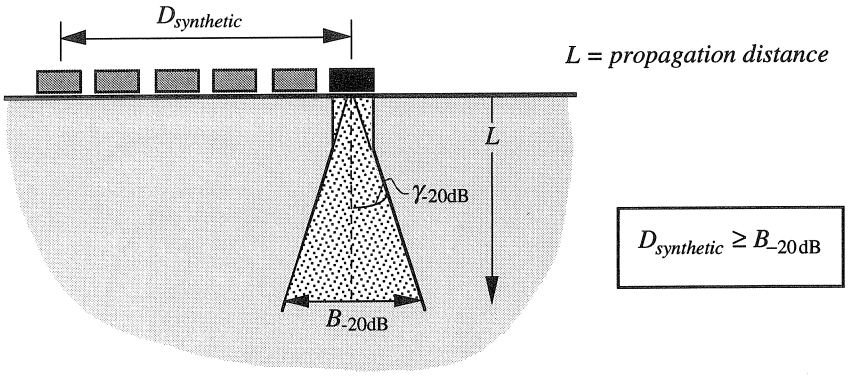

Fig. 3.8. Optimum synthetic aperture size of a scanning probe, from (Johnson 1982).

As testing distance increases, more reflected wave paths become available. These wave paths manifest themselves in the SAFT image as "echo-indications". Fig. 2.28b shows the shifted B-scan for the 5–6 reflection path. Other paths present in the time window of Fig. 2.28b, such as the 4–5 and 5–8 reflection paths, have only a slightly different time-shift function. The strongest indication in the image results from the coherent sum of the 5-6 reflection path. The coherent sum of the 4–5 and 5–8 reflection paths form the echo-indications in the SAFT image of Fig. 3.9e.

Despite the poor resolution in SAFT images from long-distance pulse-echo testing, the images still reliably detect and locate the crack. Visual interpretation of a pulse-echo SAFT image facilitates analysis of pulse-echo data, however the ambiguity of the indications resulting from a limited aperture size must be kept in mind when interpreting the images.

The image in Fig. 3.9e illustrates another feature of SAFT-processing. Signals from this long-distance aperture, partly shown in Fig. 2.28a, have a very low signal-to-noise ratio. Despite the low signal-to-noise ratio, the image still provides sufficient visual detection capabilities. The SAFT process filters out noise from the weak long-distance signal to allow better interpretation of the data. This additional feature of SAFT makes it preferable in evaluating long-distance data.

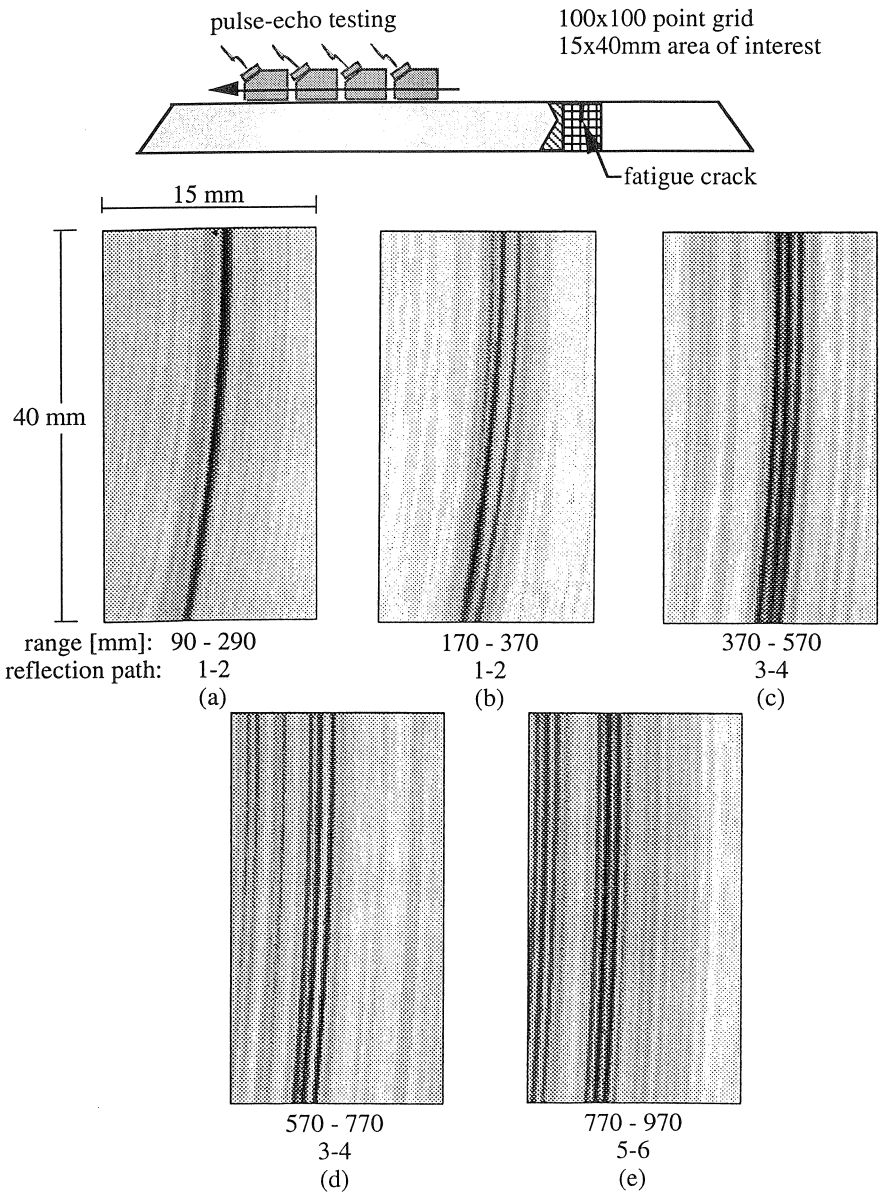

Fig. 3.9. SAFT images using a 200 mm aperture from different pulse-echo testing ranges.

3.1.2 SAFT-imaging from pitch-catch measurements

Pitch-catch configuration measurements of a normally-oriented defect give a higher signal-to-noise ratio than pulse-echo configurations because of the shorter wave path associated with the separate source and receiver. This feature of a decoupled source and

receiver also provides SAFT images from pitch-catch measurements with better resolution than images from pulse-echo measurements.

Resolution of points through the thickness of a plate requires non-coincident equidistant ellipses for the offset positions in the aperture. To obtain non-coincident ellipses in the illuminated layer, the curvatures of the ellipses from each offset position must vary sufficiently. In pulse-echo testing only larger apertures can increase the total variance of ellipse sizes. In pitch-catch testing, the ellipse curvature at each position in the synthesized aperture can change more rapidly depending on the probe configuration.

Fig. 3.10 shows the ellipse of equidistant path lengths for a pitch-catch probe configuration with a 1–2 reflection path to and from a normally-oriented defect. As with pulse-echo layer idealization, the probe positions define the major axis of the ellipse and its foci. The propagation distances l_1 and l_2 again determine the total ellipse size. Keeping the source position constant, measurements from scanning of the receiver probe contribute to the synthetic aperture in pitch-catch testing.

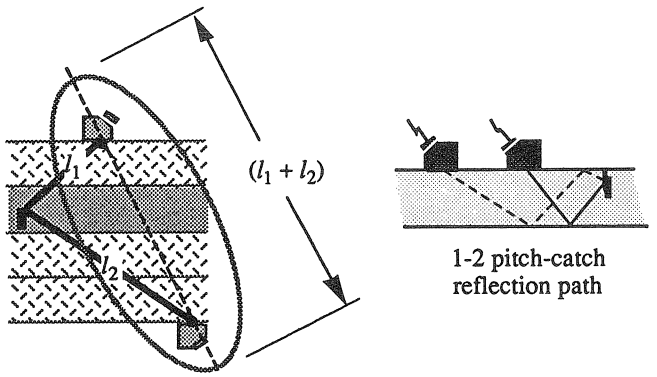

Fig. 3.10. Ellipse of equidistant path lengths using layer idealization of a pitch-catch 1–2 reflection path.

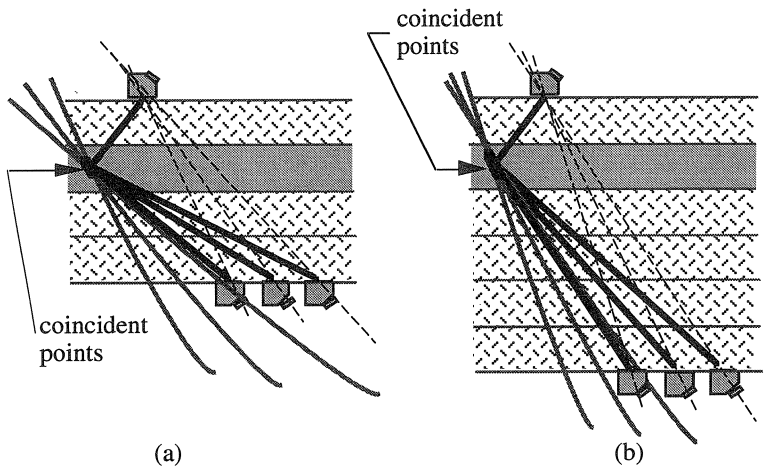

Fig. 3.11. Ellipses of equidistant path lengths for different pitch-catch receiver offset positions. (a) 1–2 reflection path, (b) 1–4 reflection path.

Fig. 3.11 shows ellipses of equidistant paths for a scanning pitch-catch receiver. Longer propagation distances in the 1–4 wave path produce larger ellipses than with the 1–2 wave path. As the offset increases, not only does the ellipse size increase, but its axis angle changes. With the larger propagation distance, increases in offset have less effect on the angular orientation of the ellipse. At longer propagation distances, small changes in the ellipse within the illuminated layer yield more coincident points resulting in less resolution in the SAFT image.

Fig. 3.12 presents SAFT images from pitch-catch testing at increasing distances. The 10 mm deep surface-breaking fatigue crack, imaged in the previous section with pulse-echo, is imaged in Fig. 3.12. The images in Fig. 3.12b–d have 200 mm apertures and use the pitch-catch testing configuration in Fig. 2.25. The image in Fig. 3.12a uses a transmitting distance of 165 mm and has a 200 mm aperture except for the close range measurements from 200 mm–300 mm. The images represent a 15 mm × 40 mm section of the plate centered around the crack, generated using a 100 × 100 point grid.

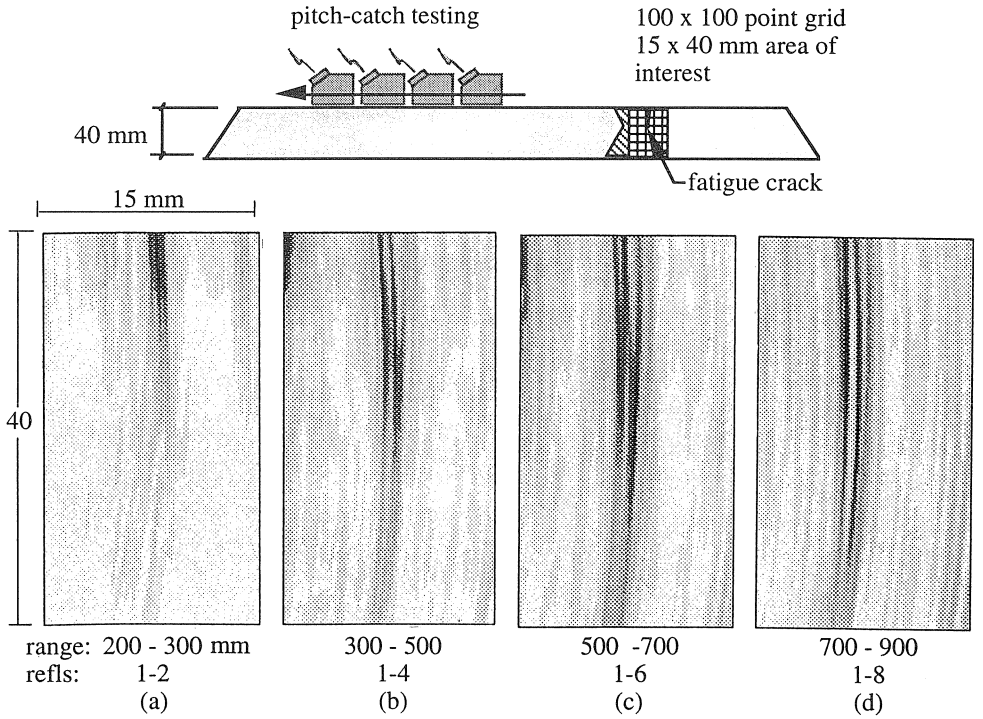

Fig. 3.12. SAFT images from a pitch-catch testing configuration on a 40 mm plate with transmitting probe positioned at 165 mm offset.

Pitch-catch testing has the possibility of providing accurately finding the depth of a defect from close ranges. Fig.3.12a shows good depth resolution of the crack from a receiver distance range of 200 – 300 mm. As the propagation distance increases, resolution decreases as with pulse-echo testing. Once again, detection and lateral resolution remains very good, even when testing from 900 mm.

3.2 *Crack growth by SAFT image energy*

SAFT images derived from both pitch-catch and pulse-echo long-distance testing show indications with excellent lateral resolution and poor depth resolution. Defects are detected and located from SAFT images when testing from distances up to 1.0 m. Despite the lack of visual depth resolution in a long-distance SAFT image, quantitative analysis of the SAFT image can provide information concerning the defect size.

A quantitative analysis of a SAFT image requires an analytical description of the processing technique. Langenberg (Langenberg 1987) discusses SAFT-imaging within the context of general inverse scattering problems. The forward scattering problem finds the scattered response when an inhomogeneity in a solid is subject to an incident wave field. The inverse scattering problem, the complement of the forward problem, characterizes the inhomogeneity given the scattered response and the incident wave field. SAFT-imaging solves the inverse scattering problem under specific boundary conditions for the source and receiving surface geometry. Using the notation in (Langenberg et al. 1986) the total field Φ resulting from a source at position $\boldsymbol{R}_0$ in the presence of a scatterer $\gamma(\boldsymbol{R}')$ with volume V as in Fig. 3.13 is

$$\Phi = \Phi_i + \Phi_S$$

where Φ_i is the incident wave field and Φ_s is the scattered wave field.

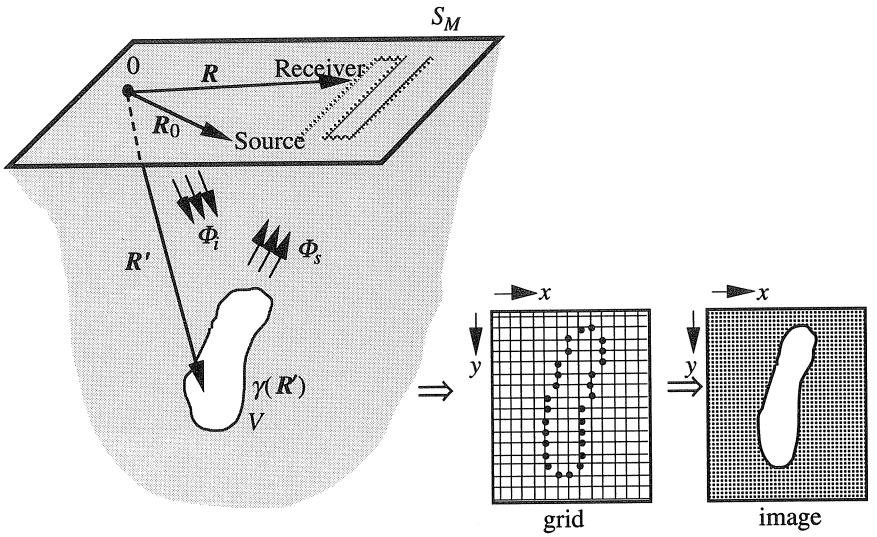

Fig. 3.13. The SAFT-imaging process. Scatterer γ ($\boldsymbol{R}'$), measurement surface S_M, incident wave field Φ_i, and scattered wave field Φ_s produce a grid of points which can be converted into an image of a defect.

The scatterer $\gamma(\boldsymbol{R}')$ produces a continuous, secondary source field Φ_B that depends on the incident field. The scattered field at a single observation point with position $\boldsymbol{R}$ is found by integrating over the volume of the scatterer.

$$\Phi_S(\boldsymbol{R}, t) = \iiint_V \Phi_B(\boldsymbol{R}_0, \boldsymbol{R}', t)\, d^2\boldsymbol{R}' \tag{3.1}$$

Ultrasonic testing of plates, as described earlier, uses a single measurement surface to transmit and receive the wave fields. Fig. 3.13 shows both the source and receiver on the same measurement surface S_M. Reconstructing the scatterer from the scattered field incident on the measurement surface S_M on a the basis of a grid of points gives an image (Langenberg 1987):

$$o_{SAFT}(x, y) = \int_{S_M} \Phi_S(\boldsymbol{R}, t)\, d^2\boldsymbol{R} \tag{3.2}$$

where $O_{SAFT}(x, y)$ is an image with pixels at x and y as in Fig. 3.13. The variable t in eqns. (3.1)–(3.2) represents the travel time function between the source, the scatterer and the receiver for each point on $\gamma(\boldsymbol{R}')$.
Pixel values in the SAFT image consist of the summation of the scan response measurements "in focus" at the pixel location. As the scattering surface $\gamma(\boldsymbol{R}')$ increases in size, the image reflects the increase in the form of larger pixel values in the image.

The response measurements used in long-distance testing, described in section 3.1, are proportional to velocity of the plate surface, v. An estimation of the total energy received in the SAFT image from a given path uses the square of the pixel values (or v^2), integrated over the image:

$$E_{SAFT} = \int_{\Psi} [O_{SAFT}(\boldsymbol{R})]^2 d\boldsymbol{R} \tag{3.3}$$

where Ψ represents the set of pixels in o_{SAFT}. Comparison of the energy estimate, E_{SAFT}, with the actual crack surface area reveals the relationship between long-distance reflected energy and growth of the normally-oriented crack.
Fig. 3.14 shows the relationship between E_{SAFT} and increasing crack surface area for pitch-catch testing. Energy in the SAFT images in Fig. 3.14 come from the pitch-catch measurements on the 40 mm plate shown in Fig. 3.12. Fig. 3.12 shows examples of the SAFT images from these pitch-catch measurements when the crack surface area reaches 666 mm^2. The source probe sends from a fixed position at 165 mm offset. The SAFT image for each measurement uses a 200 mm synthetic aperture starting at 300, 500 and 700 mm testing distances. As in Fig. 3.12 the SAFT image apertures use the 1–4, 1–6 and 1–8 wave paths respectively.

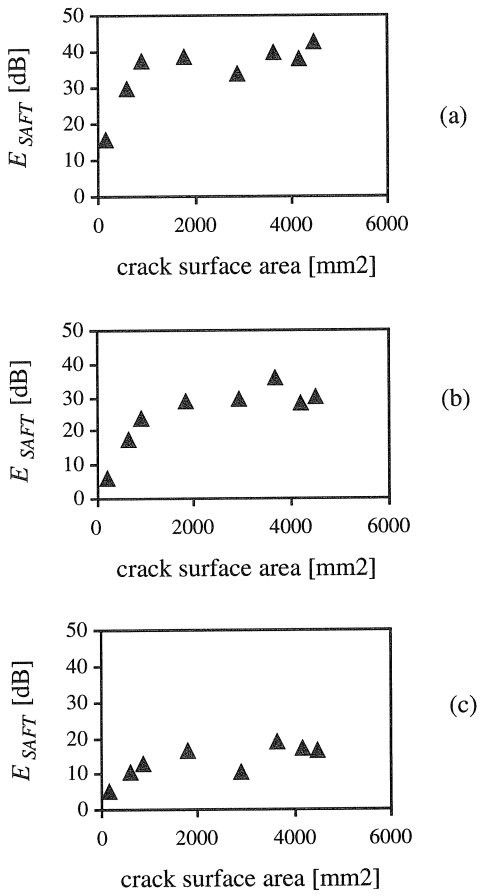

Fig. 3.14. Pitch-catch testing of 40 mm plate. SAFT image energy increases with crack surface area. (a) synthetic aperture from receiver at 300–500 mm, (b) aperture at 500–700 mm, (c) aperture at 700–900 mm.

E_{SAFT} increases with crack surface area from all three testing ranges. Comparison of Fig. 3.14 to Fig. 2.31 indicates that SAFT image energy correlates better to crack area than the maximum response from measurement at a single position. E_{SAFT} uses contributions from all measurements in the synthetic aperture resulting in better correlation with crack size. Increased crack size increases Φ_{B} in eqn. (3.1) which in turn increases o_{SAFT} in eqn. (3.3). Therefore despite the lack of visual depth resolution in the long-distance SAFT images, the quantitative measures of energy in the images provides some insight into the crack size.

Normalization of the E_{SAFT} values to that found from an image of the smallest crack size gives the relative decibel gain in energy as the crack grows. Because only a single ray is included in the SAFT image, E_{SAFT} has significance only on a relative basis. Absolute values of E_{SAFT} indicate the energy in a single ray for a given aperture. This value changes for different rays and different aperture sizes and positions. Although relative values give

a precise relative comparison, the absolute accuracy of each value in Fig. 3.14 depends on the E_{SAFT} value measured from the smallest crack. As a result all values in Fig. 3.14 should be considered strictly on a relative basis.
As testing distance increases, E_{SAFT} becomes less sensitive to crack growth. Results in Chapter 2, Figs. 2.30 and 2.31 also demonstrated decreasing sensitivity to crack growth in individual measurements for larger offset positions. In addition to the decreased sensitivity from individual traces at long-distances, sensitivity also diminishes due to the decreasing ratio of aperture size to propagation distance. However, SAFT images from an aperture at 700 mm–900 mm offset still shows good correlation to crack growth.

3.3 *Conclusions*

This chapter explores the capabilities of SAFT-processing in deriving more information from long-distance testing measurements. SAFT-imaging uses data from measurements to graphically reconstruct the defect area. The resultant image allows qualitative visual assessment of the defect. In addition to spatial filtering of data SAFT-processing acts as a noise filter, isolating the response of the chosen wave path and eliminating noise effects from the graphic representation. This added feature makes SAFT particularly attractive when processing characteristically noisy data, as found in long-distance measurements.
From testing distances of up to 1.0 m, SAFT images identify the existence and lateral location of a normally-oriented defect. This detection and location capability results from isolating a single wave path to and from the defect. In contrast to localized testing with a very limited number of wave paths, long-distance testing generates a wave field with numerous wave paths. By considering only one wave path SAFT can circumvent certain problems associated with multiple wave paths in long-distance data.
Depth resolution of a defect in a SAFT image depends on the aperture size used relative to the propagation distance of the wave path. An exact reconstruction of a defect requires an infinitely large testing aperture. Localized testing usually permits a relatively large aperture-to-propagation distance ratio and better depth resolution. With the objective of extended accessibility and limited scan distance, long-distance testing has a very small aperture-to-propagation distance ratio, resulting in very poor depth resolution of a normally-oriented defect in the SAFT image.
To obtain more information on the character of a defect from the SAFT image the parameter E_{SAFT} is introduced. This parameter attempts to compensate for the lack of depth resolution of cracks in long-distance SAFT images. The energy in the SAFT image, E_{SAFT}, gives a quantitative estimate of the magnitude of the scatterer. Images taken from long-distance measurements show that E_{SAFT} increases with incremental growth in the surface-breaking fatigue crack. Until now, only visual information from the SAFT image has been used in defect assessment. By offering a quantitative measure from the SAFT image, E_{SAFT} contributes additional information concerning the size of the defect.
Without modeling the total energy balance in the measurement process, E_{SAFT} can only determine relative crack sizes. Comparison of E_{SAFT} measurements at intervals of crack growth yields an estimate of the relative crack size. Identification of the absolute crack

size from a single scan measurement would require baseline values for the particular crack and testing configuration.
The special defect configuration used in this chapter, a normally-oriented fatigue crack in a plate, limits the applicability of E_{SAFT} in estimating crack size from scan measurements. With some obliquely-oriented cracks, E_{SAFT} may not appear to increase with crack growth. The scattered field for these types of cracks does not return to the receiving probe in the same way as the field from a normally-oriented crack. Equations for the scattered field given in this chapter apply when considering the entire scattered field. All scans cover a reduced area of the measurement surface. For an obliquely-oriented crack a larger measurement surface, or a larger scan aperture could show E_{SAFT} increasing with crack growth.

4 Modeling of long-distance testing

4.1 *Probe modeling*

The ray theory model of the plate requires a point source or a distribution of point sources at the surface to simulate excitation from a probe. Several methods can be used to derive a point source model of a probe. Previous methods involve either analytical solutions or deconvolution of measured data. The method used here is a new approach to probe modeling. Excitations on the probe face are optically measured. This results in a discrete point source model of the probe.

4.1.1 Angled *S*-wave generation

Producing *S*-waves in steel through refraction of *P*-waves requires ideal surface contact conditions between two media at their interface as shown in Fig. 4.1a. Refraction of an *S*-wave requires that the interface transfer displacements in both shear and normal directions. A contact *S*-wave probe has a gel-filled interface between the probe material and steel. This gel interface transfers only the normal components of the perspex wave field across the interface into the steel as shown in Fig. 4.1b. (Kühn, Lutsch 1961) Although both the ideal and gel interfaces result in introduction of an *S*-wave into the steel, the mechanisms which produce the *S*-wave differ between the two interface types.

A *P*-wave obliquely incident upon an ideal interface refracts and can produce both a *P* and an *S*-wave in the interfacing medium according to Snell's law. The different impedances in the two interfacing media provide the mechanism for refraction. In a perspex-steel gel interface, the lack of shear transfer across the interface prevents refraction. Generation of the *S*-wave with the gel interface occurs through a temporal delay mechanism of the normal forces and the interference of wavefronts resulting from the normal forces.

To understand this, consider a single, normally-oriented, surface point source with time-varying load $f_0(t)$. This point source produces both a spherical *P* and *S* wave front as well as a Rayleigh (*R*) surface wave as in Fig. 4.2a. Fig. 4.2b shows how a series of these normal point loads, each having a load $f_0(x, t)$, acting at the interface can generate an angled *S*-wave front. Angled *P*-waves can be generated in a similar manner with a different series of loads, $f_0(x, t)$. As evidenced in later sections of this chapter, superposition of a temporally and spatially varying series of normal point sources results in a coherent *S*-

wave propagating at angle θ. Produced strictly from normal components of the incident wave at the interface, the *S*-wave results from the time-dependent application of the normal components of the incoming *P*-wave as it impinges upon the interface. The combination of the time and space dependent functions for the probe $t(x)$ and $A(x)$, termed the source or probe function along with the time-varying load $f_0(x, t)$, yield the probe model required for input to the ray theory plate model developed later.

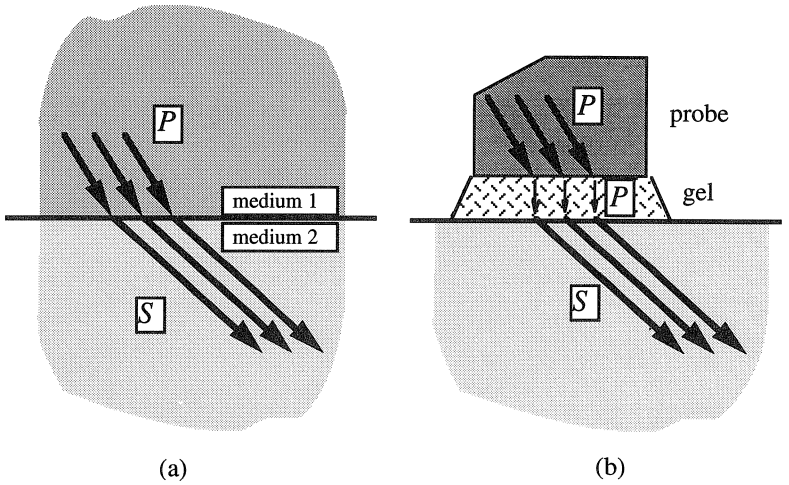

Fig. 4.1. Different mechanisms of *S*-wave generation across an ideal and a gel-filled interface between two media (a) refraction at an ideal interface according to Snell's law (b) normal displacements at a gel interface.

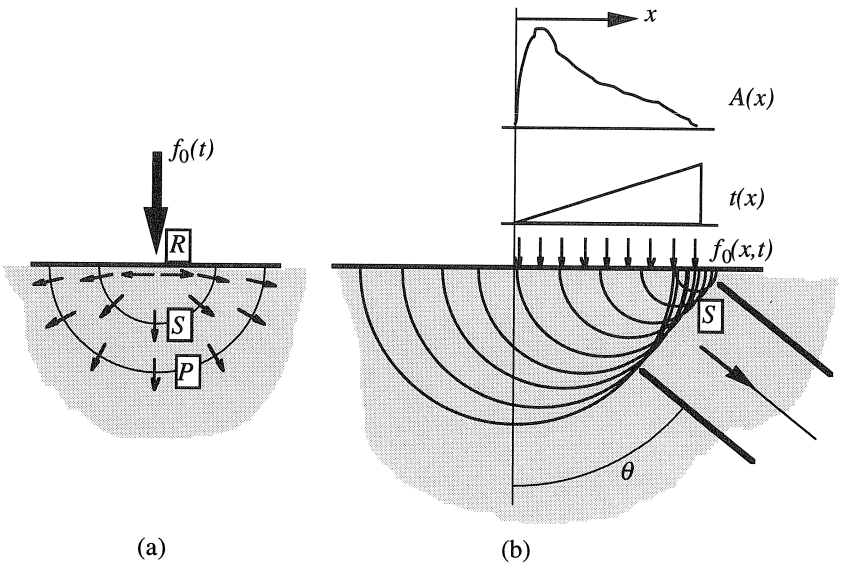

Fig. 4.2. Mechanism of *S*-wave generation at a gel interface between perspex and steel. (a) a single normal point source has *P*, *S* and *R* wave fronts (b) superposition of a series of the normal point sources produces a coherent *S*-wave. The series has both temporal and spatial dependence.

4.1.2 Direct measurements of the probe face

Recent developments in laser interferometry offer a new, relatively direct way of finding the source function of a probe. Optical laser interferometry measurements have the advantage of measuring actual surface conditions on the probe resulting in a source function that avoids numerical errors associated with deconvolution and direct integration methods. Fig. 4.3 shows the setup for the measurements. (Breeuwer, Chinn 1993; Chinn et al. 1993) The Fabry-Perot heterodyne speckle interferometer uses relative phase differences between a reference beam and a scattered field to determine the change in length of the optical path. (Vrooman 1991) When focused on the probe contact surface, the optical path of the beam length changes with the normal surface velocity. A two-dimensional scanner moves the 70° probe so that the laser focus point travels across the face of the probe in the x and y directions.

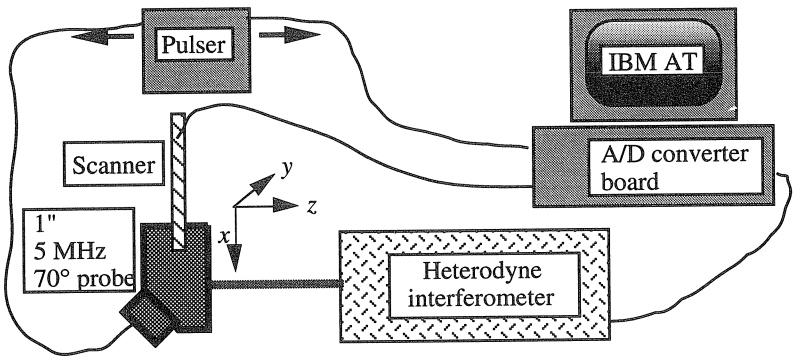

Fig. 4.3. Laser interferometry measurements of the 70° probe contact surface.

Scanning provides a picture of the spatial variation along the surface. Fig. 4.4 shows a surface plot of the particle velocities in the $+z$-direction on the probe surface at time $t = 11$ μs. The pulse stretches across the measurement area in the y-direction. The edge of the probe appears to have a noisy but incoherent profile of z-particle velocity.

The wedge used has clear perspex along the wave path and red-colored damping material outside the wave path of the transducer. The projection of the round transducer onto the wedge contact surface results in an oval shape of the clear perspex at the contact surface. This oval shape is visible in Fig. 4.4. The edge area outside the oval in the free probe surface measurements is characterized by a higher noise level than in the clear perspex area. The collection system normalizes all measurements based on the reflectivity of the returned light. The colored damping material of the wedge has higher optical reflectivity than the clear perspex oval. As a result of the normalization, the velocities outside the oval appear to have larger magnitudes than velocities inside the oval. The magnification of velocities in the edge region due to normalization is therefore deceiving.

Fig. 4.5a–4.5c show images of the probe surface at $t = 8$, 11 and 14 μs. A pulsed wave clearly moves in the negative x-direction across the face of the angled probe in time.

Fig. 4.5d shows an image of the energy found from the z-velocities in the scanned area of the probe surface. The highest amount of energy lies at the "heel" of the probe in the area having the shortest propagation distance through the wedge. A reduced area within the perspex oval, also oval shaped, shows the shape effects of the energy content.

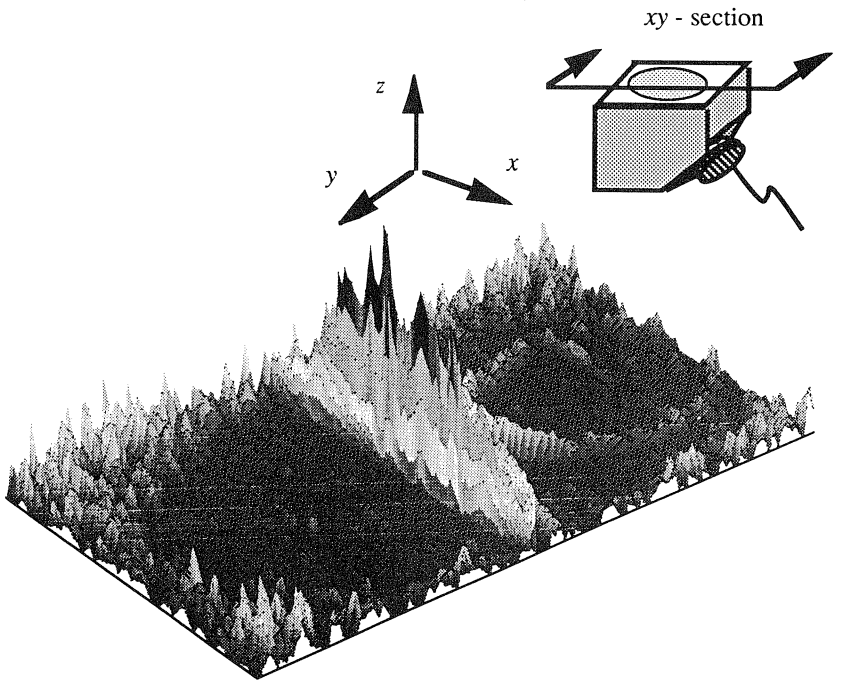

Fig. 4.4. Velocities measured on the probe contact surface at t = 7.5 μs

Fig. 4.5 shows grey-scale images of the entire scanned probe surface area at 4 time points, t = 7.5, 10, 12.5 and 15 μs. Dark areas indicate large positive velocity and light areas indicate large negative velocities with grey scales falling in between. A pulsed wave clearly moves in the negative x-direction across the face of the angled probe in time.

The amplitude of the pulse as it is incident on the probe surface varies with x-position. The frequency content of the incident pulse remains relatively constant. Fig. 4.6 shows the amplitude and peak frequency of the pulse at the y-centerline of the probe as well as the arrival time of the pulse. To minimize noise in the pulse profile, Fig. 4.6 shows the velocity and peak frequency averaged over a y = 10 mm strip of the probe, centered about the y = 15 mm axis of the scan area. Normalized maximum velocities show the increase and decrease of the pulse amplitude such that the peak velocity on the surface has a value of 1.0. All three profiles show a 45 mm x-range corresponding to the 45 mm length of the perspex oval on the contact surface.

Fig. 4.6c shows that the arrival time of the pulse decreases linearly with x position. This linear relationship along the surface results from the travel time of the P-wave through the wedge. In Fig. 4.6a the pulse amplitude decreases with propagation distance through the wedge. This results from scattering attenuation of the pulse as it travels through longer distances in the wedge. The peak amplitude occurs at approximately $x = 37$ mm, or at the area of the probe having the shortest propagation distance through the wedge.

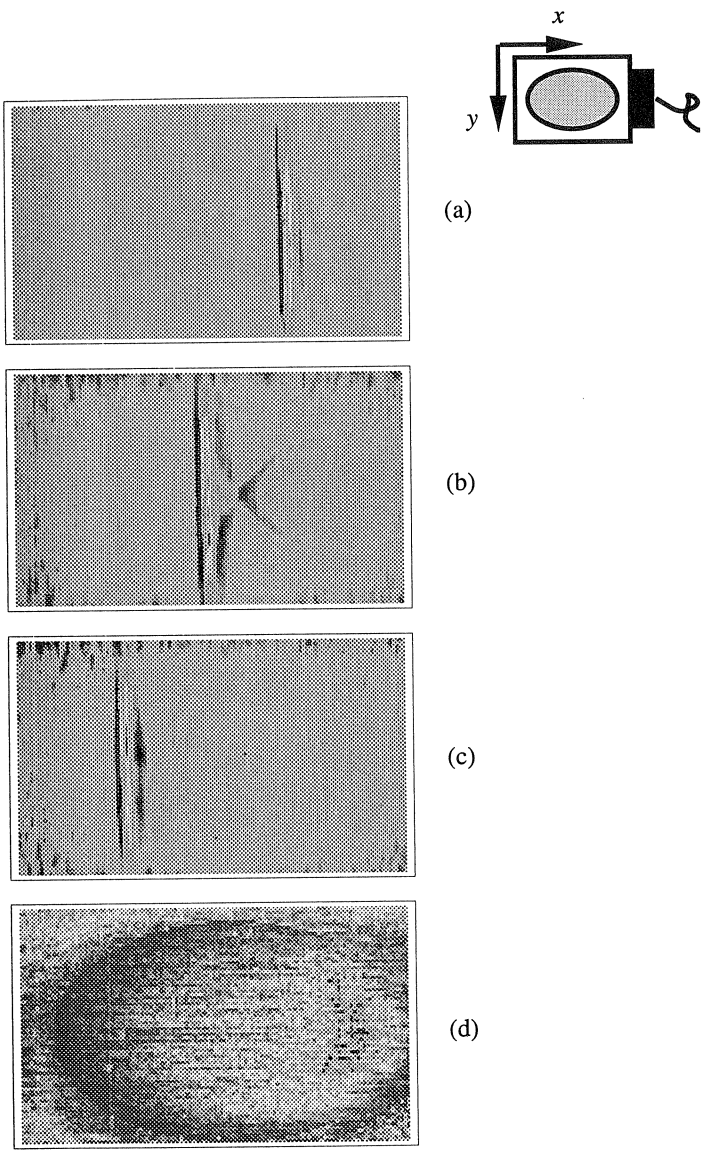

Fig. 4.5. B-scan images of velocity measurements (a) at $t = 8$ μs, (b) $t = 11$ μs, (c) $t = 14$ μs, (d) measured energy on probe contact surface.

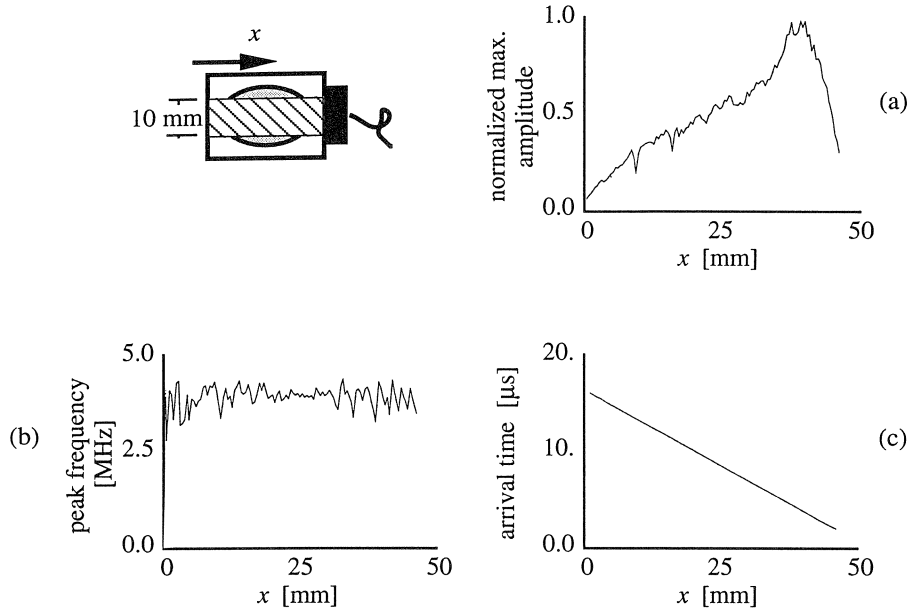

Fig. 4.6. Pulse characteristics on the 70° probe contact surface averaged over a 10 mm strip of the surface (a) normalized maximum amplitude profile (b) peak frequency profile (c) arrival time.

4.2 *Model of through-transmission testing*

Modeling through-transmission offers an opportunity to test components of the model. Without the presence of a defect, the through-transmission model can help to characterize and analyze the behavior of each component. Comparison of the modeled response to plate measurements also helps assess the use of optical measurements in developing the source function.

Laser interferometry measurements in the previous section confirm that the source function of the probe has both temporal and spatial dependence. The time function identified earlier as $t(x)$ varies linearly over the contact surface and results from the shape of the wedge in the probe. The spatial amplitude function $A(x)$ is influenced by both the propagation distance through the wedge and the projected shape of the circular transducer onto the wedge contact surface. The time-varying load $f_0(x,t)$ maintains a relatively constant peak frequency on the contact surface and is hereafter taken to be constant in space for the calculations, thus $f_0(t)$.

Combination of these source profiles provides the probe model required. The Green's function of the plate, which describes the transfer of stresses from one point in the plate to another, is found with ray theory. The Green's function provides the plate model. All calculations of plate Green's functions in this chapter use either the computer program GPLATE (Hsu 1985), provided by the National Institute of Standards and Technology (NIST), USA, or the program PLATE (Pao 1977), provided by Cornell University. Both programs find the Green's function in terms of displacements resulting from a unit step

function. Ref. (Proctor et al. 1983) provides a validation of PLATE for glass plates with known source functions. GPLATE has been validated with the examples in (Proctor et al. 1983).
Although surface normal point sources generate *P*, *S* and *R*-waves as in Fig. 4.2a, only *S* and *R*-waves propagate coherently from a 70° probe (see section 4.1). Using ray theory to model the plate response offers the advantage of selecting only those rays important to the Green's function. Modeling 70° through-transmission testing, therefore requires the inclusion of only *S* and *R*-waves in the Green's function. The Green's function, using ray theory is

$$G(\boldsymbol{x}, t) = \sum_{i=1}^{n} G_i(\boldsymbol{x}, t) \tag{4.1}$$

where $G_i(\boldsymbol{x},t)$ is the response due to ray *i*. For the model, we consider ray *i* as either *S* or *R* rays that arrive within the time period under consideration.
Convolution of $G(t)$with the time-varying load $f(t)$ gives the displacement response by the equation:

$$u(\boldsymbol{x}, t) = \dot{G}(\boldsymbol{x}, t) \cdot f(t) \tag{4.2}$$

The time-varying load $f(t)$ represents the source function. Inclusion of the probe function into $f(t)$ uses all three components found in the previous section or

$$f(t) = f(A(x), t, (x), f_0(t)) \tag{4.3}$$

The measurement system records a response corresponding to the particle velocity of the surface. For comparison to measurements, the model must calculate the modeled velocity response. Velocity calculations follow from eqn. (4.2) according to

$$v(\boldsymbol{x}, t) = \ddot{G}(\boldsymbol{x}, t) \cdot f(t) \tag{4.4}$$

Commutative properties of derivatives in convolution (McGillem, Cooper 1974) allow eqn. (4.4) to be written

$$v(\boldsymbol{x}, t) = G(\boldsymbol{x}, t) \cdot \ddot{f}(t) \tag{4.5}$$

for a linear, time-invariant system.

4.2.1 Multiple point source modeling

Laser interferometry measurements described earlier provide a picture of the probe surface at discrete points. Because discrete rays are used in the calculation of the Green's function, a discrete, multiple source model is easily applied to the ray theory model of the plate.

Fig. 4.7 shows a model of the 70° send probe using multiple point sources spaced over 45 mm surface length. The sending probe model has three components. Each point source applies the time-varying load $f_0(t)$ found from the laser measurements. Application of each point source occurs in sequence according to the linear time delay $t(x)$ shown in Fig. 4.6c. The maximum amplitude of $f_0(t)$ at position x varies according to $A(x)$ as shown in Fig. 4.6a.

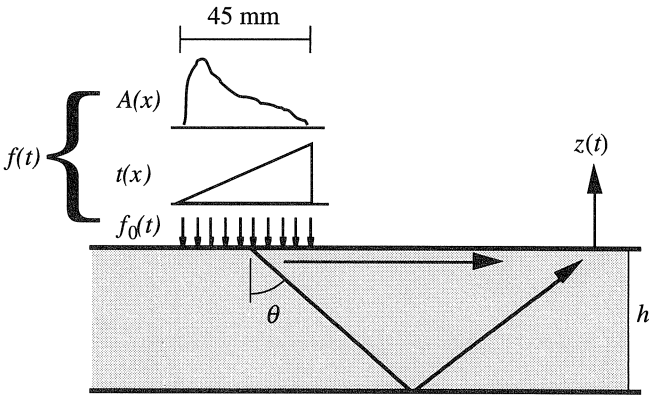

Fig. 4.7. Multiple source – point receiver model of through-transmission testing.

Summation of the rays according to eqn. (4.1) yields the complete Green's function of the plate. Multiple sources require the summation of the responses from each source. Fig. 4.8 gives the ray responses at different steps in the summation. Fig. 4.8a shows the velocity response due to $f_0(t)$ for a series of 10 point sources configured as shown with $\theta = 60°$ at the center of the series. The responses only include the effects of the $f_0(t)$ component of the source, the functions $A(x)$ and $t(x)$ are constant and have no spatial variation in this plot.

Including the linear delay $t(x)$ in $f(t)$ gives the B-scan set shown in Fig. 4.8b. Summation of the 10 separate responses and inclusion of $A(x)$ to $f(t)$ gives the velocity trace in Fig. 4.8c. The profile of peaks in the summation of Fig. 4.8c follow the profile of $A(x)$.
Directional effects of the probe result from diffraction of the field at the probe-plate interface. Interference of the diffraction effects causes the directional behavior of the probe. Simulation of these diffraction effects requires that the same interference phenomenon occurs in the model. The spacing of the point sources along the surface is critical to simulating these interference effects. The probe model must be sufficiently discretized to simulate interference. When the point sources are placed too far apart, not enough interference occurs between the fields of the point sources to create the correct directional effects.
Fig. 4.9 shows the effect of discretization on the source model for 1, 10, 40, 60 and 100 point sources. All three components $A(x)$, $t(x)$ and $f_0(t)$ are included in these summations. Spacing of the source points shown in Fig. 4.9a varies from 0.5 λ to 56 λ for 100 to 1 source point respectively.

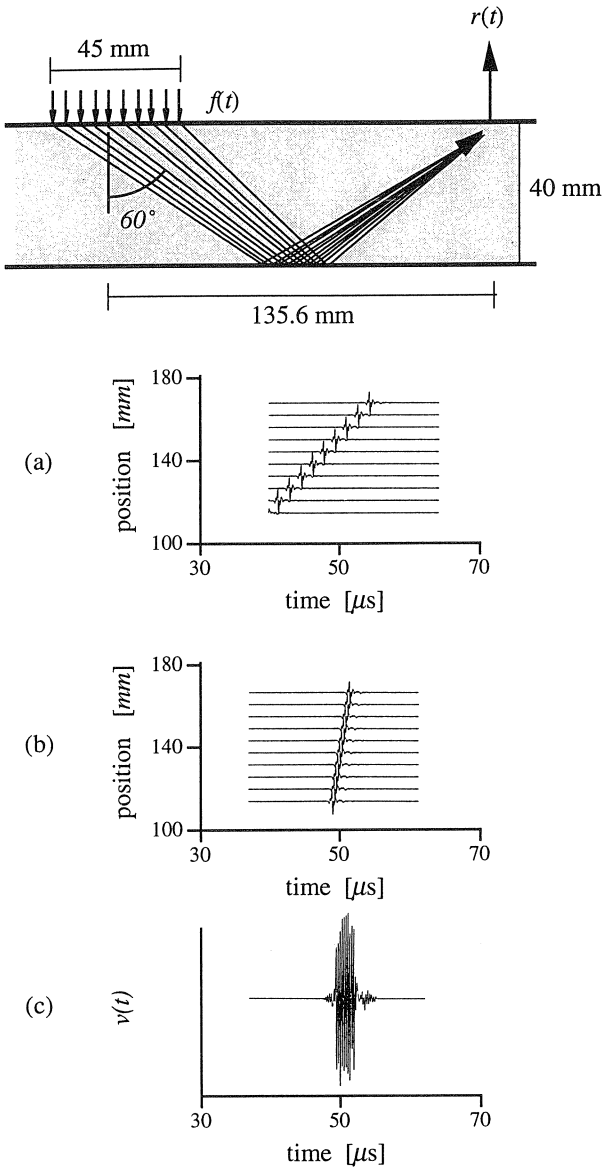

Fig. 4.8. Modeled velocity response using a 10 point source (a) B-scan response (b) response including $t(x)$ and $A(x)$ (c) summed 10 point source response.

Summed traces from each of the sources are shown in Fig. 4.9b. The single source (n = 1) response has the same shape as $\ddot{f}_0(t)$ and does not include any interference effects. The 10 and 40 point sources also resemble $\ddot{f}_0(t)$ indicating that source spacing larger than 1.4 λ does not provide sufficient interference in the resultant wave field. Only when the source contains 60 or 100 points, i.e. with spacing of λ or smaller, do interference effects

begin to smooth out the traces. The response from the $n = 60$ and $n = 100$ point sources appear closer to a measured surface wave than the input load $\ddot{f}_0(t)$. A multiple point source therefore requires spacing of at most λ to correctly model interference effects.

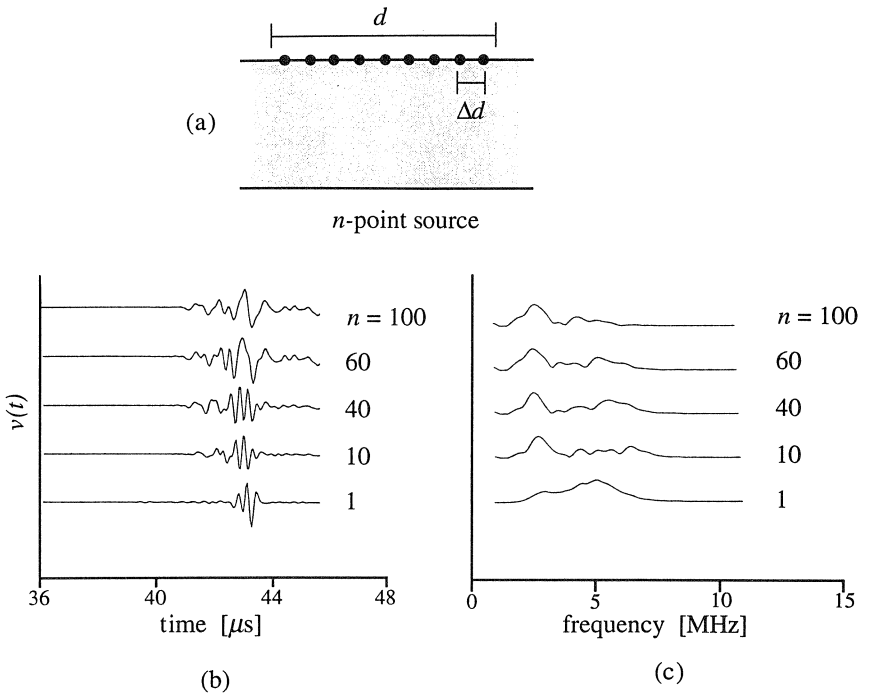

Fig. 4.9. Discretization effects of an n-point source at 60° (a) point source spacing (b) velocity response for each n-point source type (c) frequency response for each n-point source type.

Fig. 4.9c presents the effects of source discretization on the frequency content of the velocity response. The frequency spectra indicate that by changing from a single source to a multiple point source, the peak frequency changes from 4 to 1.7 MHz. This peak frequency shift results from the effective convolution of the combined time delay function $t(x)$ and the amplitude function $A(x)$ with the single source velocity response $\ddot{G} \cdot f_0(t)$. Combining eqns. (4.3) and (4.4) gives

$$v = \ddot{G} \cdot (At \cdot f_0)$$

Using associative laws of convolution (McGillem, Cooper 1974), we rewrite this equation as

$$v = At \cdot \ddot{G} \cdot f_0 \tag{4.6}$$

or

$$v(t) = H(t) \cdot F(t) \tag{4.7}$$

where $H(t) = A(x)t(x)$ and $F(t) = \ddot{G} \cdot f_0(t)$.
Fig. 4.8b shows $v(t)$ from eqn. (4.6) including the time delay function $t(x)$ and the amplitude function $A(x)$ at 60°. Applying the time delay $t(x)$ causes the pulse to occur within a time span of Δt ~1.2 μs as in Fig 4.10a. Summing these traces to obtain the complete probe wave field constitutes a convolution. In the frequency domain the convolution represents a multiplication of the Fourier transform of $H(t)$ with the Fourier transform of $F(t)$. Assigning $H(\omega)$ and $F(\omega)$ to the Fourier transforms of $H(t)$ and $F(t)$, respectively, we write the Fourier transform of the summation as

$$\mathrm{F}[\Sigma v(t)] = F(\omega) H(\omega) \tag{4.8}$$

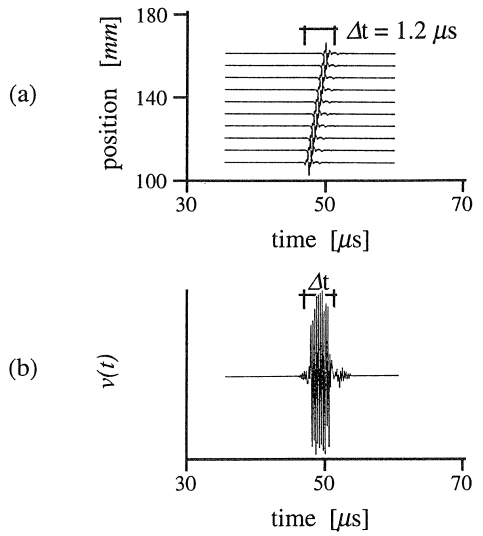

Fig. 4.10. Summation of the point source responses (a) pulse responses fall within the time period Δt (b) the summation of responses approaches a square pulse of width Δt.

The time shift Δt determines the extent of shift in the peak frequency when moving from a single to a multiple point source. A 70° probe has a directionality such that $|\Delta t|$ is minimized for 70° wave propagation. An off-axis nominal wave angle of $\theta = 60°$ propagating from a 70° probe results in a time shift of Δt = 1.2 μs. As the propagation angle from the source approaches 70°, the pulse width $|\Delta t|$ becomes smaller. The broadened frequency spectra of $H(\omega)$ results in less shift in the peak frequency. This frequency analysis offers more insight into the mechanism behind the directionality of the angled probe. Subsequent sections discuss directionality of the probe resulting from the pulse width Δt.
Modeling through-transmission testing using 70° source and receiving probes would require at least a fully discretized source and receiver as in Fig. 4.11. In addition, the surface response $z(t)$ would need further convolution with the probe functions $t_{receive}(x)$ and

$A_{receive}(x)$, representing the reverse propagation through the wedge to the receiving transducer. To avoid excessive computation time, the following section develops a simplified model that uses the mechanisms found in this and the previous section.

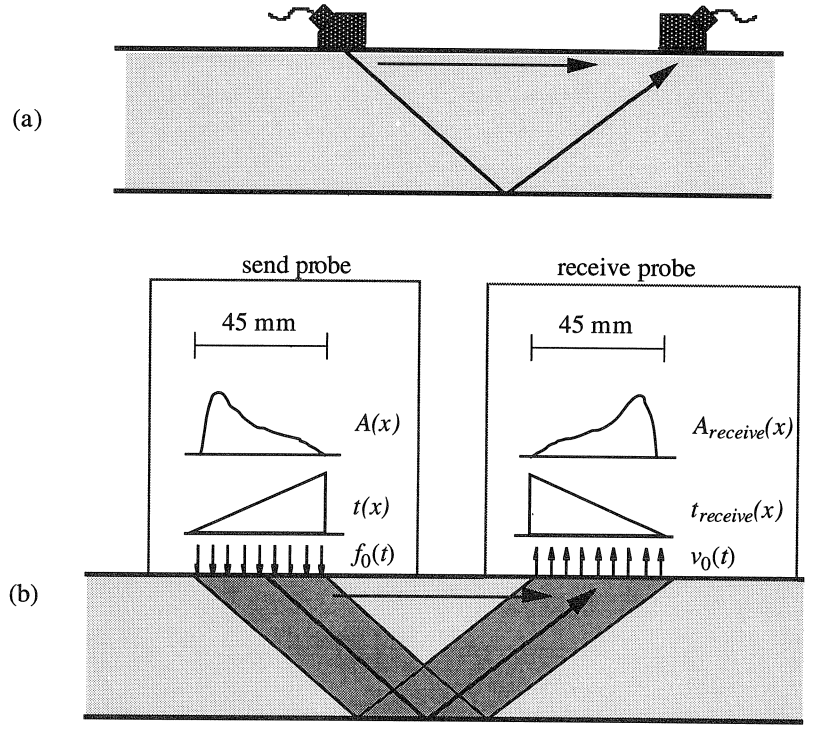

Fig. 4.11. Measurement and modeling of through-transmission testing using angled probes. (a) measurement configuration (b) multiple point source and receiver model.

4.2.2 Modeling probe directionality

The duration of the response, Δt, using the multiple point source model determines the shift in peak frequency at off-axis positions. From conservation of energy, the amplitude of the off-axis pulse response also depends on the duration Δt. Towards developing a simplified model for the probe, this section examines the relation between the pulse duration Δt and the directionality of the probe.

Ignoring both the spatial variation component of the probe, $A(x)$, and the phase information given by the time-varying load $f_0(t)$, the pulse duration, Δt, can singly describe most of the directionality aspects of the response. The rectangular pulse in Fig. 4.10b represents the summation of impulse responses from a continuum of point loads at the source. To generate the rectangular pulse for $v(t)$, $m \rightarrow \infty$ in Fig. 4.11b and only $\ddot{G}(t)$ in eqn. (4.4) is required if we assume that $f_0(t)$ is a Dirac δ function.

The difference in arrival times of the point sources, less the wedge delay $t(x)$, determines the duration of the square pulse. Fig. 4.12 shows a model of the probe using only the linear delay function and the plate ray propagation time. Contained in a continuum of sources that simulate a probe with contact surface length D and time delay function $t(x)$,

point source M lies in the middle of the contact area at offset position x_M from the edge of the source. To reach the receiver point P on a plate of thickness h the 1-reflection S-wave must propagate at an angle θ_M and cover a surface offset distance of r_M arriving at time $t_S = t_S(x_M)$.

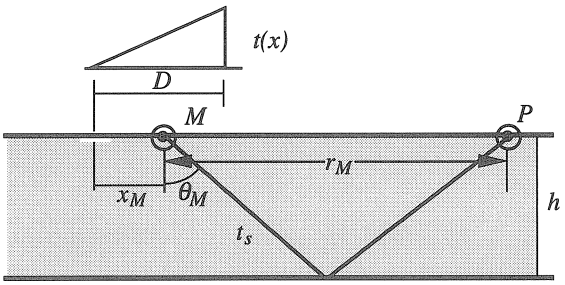

Fig. 4.12. Linear delay model of an angled probe.

Using a multiple source – point receiver model, calculation of the pulse duration based strictly on

$$\sum \ddot{G}(t)$$

follows the equation:

$$\Delta t = \max(t_S(0) - t_S(x) - t(x)) - \min(t_S(0) - t_S(x) - t(x)) \tag{4.9}$$

for the range $x = 0$ to $x = D$. For a fixed receiver point, the angle of propagation is related to offset or $x(\theta)$.

Because the receiving transducer has a constant size, we can assume a constant value of or the area under the rectangular pulse as in Fig. 4.13. The duration of the pulse therefore has an inverse relation to its height and the peak amplitude of the velocity $V(\theta)$ can be described by

$$V(\theta) \propto \frac{1}{\Delta t(\theta)} \tag{4.10}$$

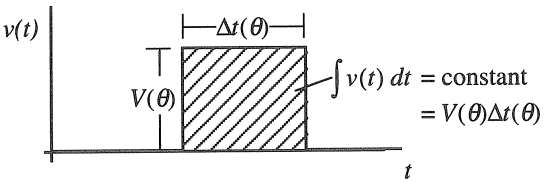

Fig. 4.13. Square pulse with duration $\Delta t(\theta)$.

Fig. 4.14 shows the inverse of the pulse duration, $1/\Delta t$, for a 1-reflection S-wave propagating from a continuous source to a receiver modeled with 15 points. The source has

time delay $t(x)$ corresponding to a 70° angled probe. For comparison the figure also includes the measured amplitude curve from Fig. 2.16 that uses 70° probes in through-transmission to both send and receive.
The linear delay model using a point receiver shows a highly directional amplitude profile, much like that expected from a focused probe. When integrated over a finite receiver area, the inverse pulse duration shows excellent agreement with measured velocity amplitudes.

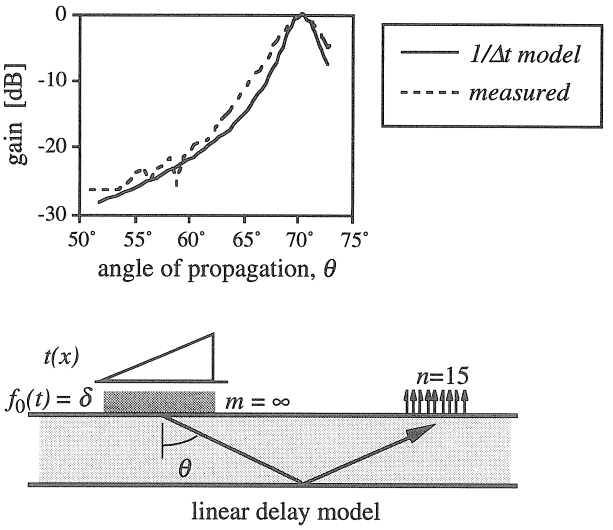

Fig. 4.14. Through-transmission testing, measured and modeled with the linear delay model containing a continuous source and a 15 point receiver.

Good agreement between the linear delay model and measurements in through-transmission testing indicate that the linear time delay function introduced by the probe, Δt, constitutes the primary mechanism behind angled probe directionality. The function $t(x)$ describes the projection of the P-wave in the wedge onto the wedge-steel interface.
The delay function is critical to modeling relative changes in the amplitude of the response between offset positions. Other spatial and time-varying components of the probe function, derived here from optical measurements, affect modeling of the absolute amplitude and frequency of the response. Simulations of single measurements with ray theory must use a fully discretized source and receiver model that includes the spatial, time-varying load and the time delay components of the probe.

4.3 *Model of defect testing*

Measurements described in Chapter 2 show that both pitch-catch and pulse-echo testing can successfully detect fatigue cracks from long distances. Limited to experiments with normally-oriented surface cracks, pitch-catch testing is more sensitive to growth of the cracks. Modeling the test system provides a reference for measurements and also pro-

vides insight into the detection process. This section uses information from measurements to develop a simplified model of long-distance ultrasonic testing.

4.3.1 Ray path energy

In the pulse-echo testing configuration shown in Fig. 2.25 a 40 mm thick plate containing a normally-oriented, surface-breaking fatigue crack has a 70° probe moving from 165–900 mm. As stated in section 3.4.1 the response measured from fatigue cracks of this type consist mainly of reflected energy. The small amount of diffraction energy from the crack tip is not visible in the presence of reflection energy from the normal crack face.

Four unique reflection ray paths arise when considering measurements with the probe positioned between 300–500 mm. Fig. 4.15 shows the 1–2, 1–4, 2–3, and 3–4 paths possible from these positions. Again, a 1-2 reflection path has 1 plate surface reflection on the path to the defect and 2 surface reflections on the return path. Because a 1–2 reflection path has a travel time equal to a 2–1 reflection path the 1–2 reflection path here refers to both the 1–2 and the 2–1 paths. Given the smooth surfaces of the plate used in measurement, all paths to and from the crack assume specular reflection at the surface as in Fig. 2.24a, without scattering of rays. At a given offset position x, each of the paths must follow various propagation angles in order to satisfy specular reflection conditions at the plate surface.

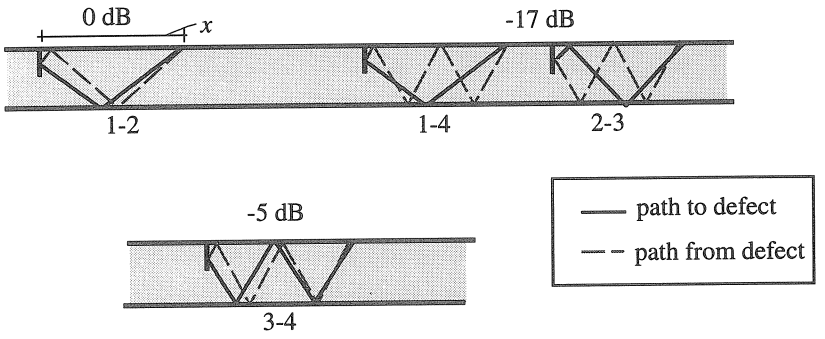

Fig. 4.15. Relative energy of pulse-echo 1–2, 1–4, 2–3 and 3–4 ray paths at offset position x.

Different amounts of energy return to the probe along each ray path reflected by the crack. Section 4.2 describes the use of a SAFT image to estimate the energy reflected by a crack. Generated from a single path, the SAFT image energy, E_{SAFT}, provides a good estimate of the relative energy in each ray path. Fig. 4.15 also shows the different energy levels of the four paths relative to the 1–2 path in dB. The crack configuration makes it impossible to distinguish between the 1–4 and 2–3 ray paths because they have approximately the same travel time. The largest amount of energy returned to the probe comes from the 1–2 path. The 3-4 path has only 5 dB less energy than the 1–2 path. Despite having shorter path lengths than the 3–4 path, the 1–4 and 2–3 paths surprisingly have less energy with a 17 dB decrease.

4.3.2 Ray theory modeling of the reflected path

Specular ray paths from fatigue cracks deliver the highest reflection response and therefore are of most interest in long-distance testing. Normally-oriented fatigue cracks present a specific case wherein ray theory can easily model specular reflection ray paths. Fig. 4.16a presents a simplified model for pulse-echo testing of a surface-breaking, normally-oriented crack with a 1–2 ray path. At the crack surface $\theta_{incident} = \theta_{reflected}$ for the specular reflection ray path. A 3-reflection through-transmission path can model the 1–2 specular reflection path for this particular crack orientation. The plate model for a probe at pulse-echo offset distance x from the crack consists of a 3-reflection through-transmission path with source-receive distance $2x$. Modeling the response of the 1-2 pulse-echo path entails calculating the 3-reflection ray theory response.

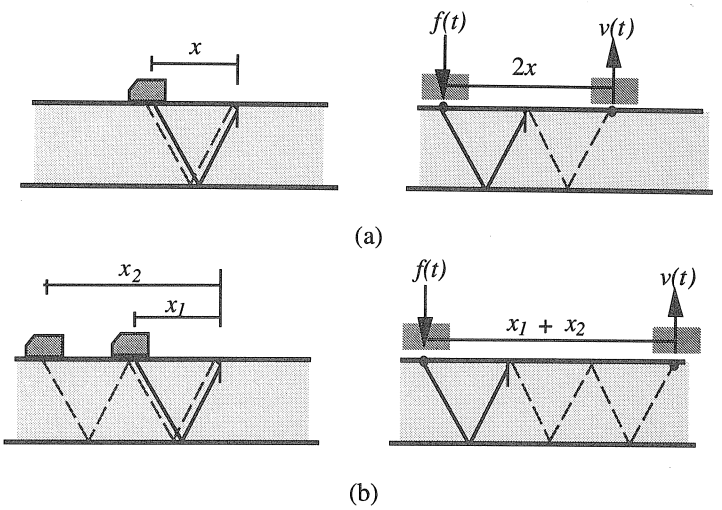

Fig. 4.16. Simplified through-transmission model of specular reflection paths from a normally-oriented surface-breaking crack (a) pulse-echo testing (b) pitch-catch testing.

The simplified model for pulse-echo testing requires that reflection from the crack occur very near to the surface of the plate. This limitation results from the requirement of approximately equal surface offset distances of the transmit and return paths. In pulse-echo testing this offset distance cannot exceed the contact surface length of the probe. A similar model for pitch-catch testing does not have this limitation due to the separate source and receiver.

Fig. 4.16b shows a simplified model for pitch-catch testing. The 1-4 specular reflection path in pitch-catch testing of a normally-oriented crack can be modeled with a 5-reflection through-transmission ray path. A transmitter offset distance of x_1 and a receiver offset at x_2 results in a modeled through-transmission offset distance is $x_1 + x_2$.

Scattered ray paths cannot be modeled this way. However, as shown in the previous section, most of the energy detected from a crack of this configuration returns along the specular reflection path. Inclusion of all specular reflection ray paths in the plate model would account for most of the energy returned from the crack.

Fig. 4.17a shows the measured pulse-echo response from a 10 mm deep normally-oriented, surface-breaking fatigue crack in a 35 mm thick plate. A 350 mm offset distance separates the crack and the probe. Fig. 4.17b shows the response using the simplified ray theory model of the same configuration. The model includes the 1–2, 3–4 and surface *R* ray paths. The additional wave arriving at ~ 226 ms in Fig. 4.17a has not been modeled in Fig. 4.17b.

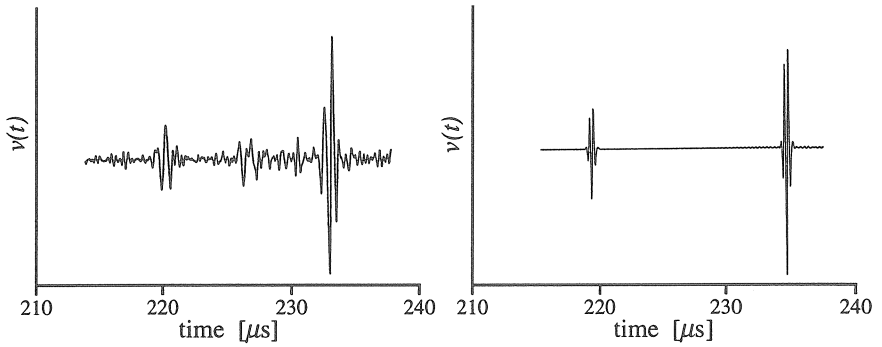

(a) (b)

Fig. 4.17. Pulse-echo response at x = 350 mm (a) measured (b) simplified ray theory model.

The arrival times of each ray path correspond very well with the arrival times of the experimental pulse-echo paths. However, the pulse shapes of the responses are not in agreement due to the single point source function used.

4.4 *Scanning pitch-catch testing and SAFT-processing*

SAFT-imaging of scan data, carried out entirely in the time domain, uses travel time differences in the reflected response to distinguish between possible reflector points. Generating a SAFT image of the defect area entails focusing successively on different points in the area under investigation. In focusing, the actual pulse shape of the received signal is of less importance than the consistency of the pulse shape over different scan positions.

4.4.1 Model of scanning pitch-catch testing and SAFT-processing

Absolute agreement of the pulse shapes derived using the ray theory model, developed earlier in this chapter, and the measured response depends entirely on the probe model used. However, arrival times of the pulses in the model agree with measured arrival times regardless of the accuracy of the probe model. Therefore despite differences in pulse shapes between the measured pulse-echo response and the modeled response, the simplified defect testing model can still be used in SAFT-imaging. Using the same probe function at each modeled offset position produces a consistent pulse shape within a simulated scan data set.

Fig. 4.18 shows SAFT images generated using pulse-echo scan measurements between 290–490 mm and the corresponding simulated scan using the pulse-echo model in

Fig. 4.16a where x = 290–490 mm. A defect with 10 mm depth is imaged using actual measured data scans in Fig 4.18a. Fig. 4.18b shows the SAFT image derived from a simulated scan of a 10 mm deep defect. Both the experimental and simulated SAFT images show a lack of depth resolution when using pulse-echo scans. The simulated scan image verifies the lateral offset of the defect found with measurements.

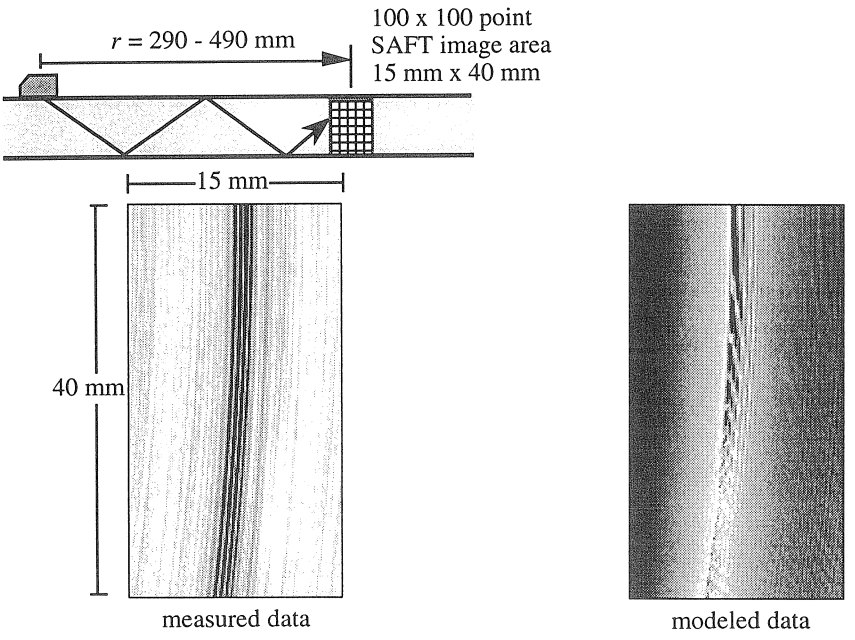

Fig. 4.18. SAFT images using the 3–4 pulse-echo reflection path testing from 290–490 mm (a) from experimental testing of a 10 mm defect (b) from simulated scan data generated using the simplified ray model.

SAFT images from pitch-catch testing generally show better depth resolution of cracks than pulse-echo testing. Fig. 4.19a shows the SAFT image derived from the 1–4 reflection path using pitch-catch testing of a 10 mm crack with the transmitting probe positioned at 165 mm and the receiving probe ranging between 290–490 mm as in Fig. 2.25. Corresponding to this pitch-catch configuration, the simplified pitch-catch model in Fig. 4.16b generates a scan data set where x_1 = 165 mm and x_2 increases from 290–490 mm.

By limiting reflector points to a certain, simulated crack depth, a comparison can be made between relative energy levels of real and simulated SAFT images. The simplified model includes only specular reflections from a defect. Unlike the pulse-echo model, the pitch-catch model does not require reflection from the crack at a point close to the top surface. A crack of depth c has reflector points only to depth c. All points in the plate thickness below point c generate zero response in the simulated scan set. Fig. 4.19b and c show the

SAFT images derived from a simulated pitch-catch data set assuming reflector points occur at points up to 5 mm and 10 mm from the surface, respectively.
As the simulated crack depth increases from 5 to 10 mm the SAFT image energy E_{SAFT}, defined earlier, increases by 5 dB. Corresponding measurements of the fatigue crack described in Chapter 2 show an 8 dB increase in E_{SAFT} when the crack depth increases from 5 to 10 mm. (Chinn 1992) Shown experimentally in Fig. 3.14 to increase with crack growth even at testing distances of up to 900 mm, E_{SAFT} is also shown here in the simplified model to increase with crack depth, even when considering only specular re flections.

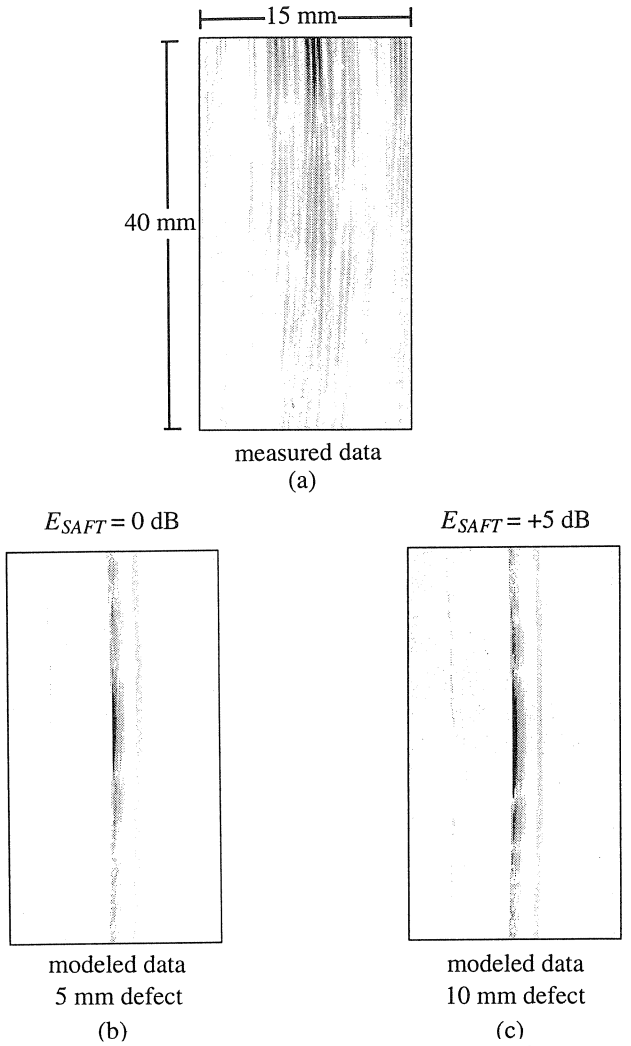

Fig. 4.19. SAFT image using 1–4 reflection in pitch-catch testing (a) from experimental scanning of a 10 mm crack (b) from a simplified ray model of a 5 mm crack (c) from a simplified model of a 10 mm crack.

4.4.2 Comparison of modeled and experimental E_{SAFT}

The simplified model of long-distance testing described in the previous sections uses ray theory to follow the propagation of the ray path to and from a defect. Limited to normally-oriented cracks with relatively smooth, non-scattering surfaces, the model so far uses crack depth and location in the plate to determine E_{SAFTT}. While this basic crack model shows increases in E_{SAFT} similar to those measured on a growing fatigue crack, the model must also consider the probe field width as the crack length exceeds the probe illumination area.

The probe used in pitch-catch measurements has a detectable (26 dB) limit of lateral spreading at 17° as in Fig. 4.20. (Chinn 1990; Chinn 1992) The transmitting probe has a beam width w_{beam} that illuminates the entire growing defect for the first few measurements. During these measurements, the crack length p_{crack} as well as the crack depth d_{crack} increase the energy returned to the receiver. After the crack length p_{crack} exceeds the probe beam width w_{beam}, the increase in the energy from the crack becomes exclusively dependent on the growing crack depth. Because of the limited probe beam width of the pitch-catch probe, the quantity E_{SAFT} varies not only with d_{crack} but p_{crack} also.

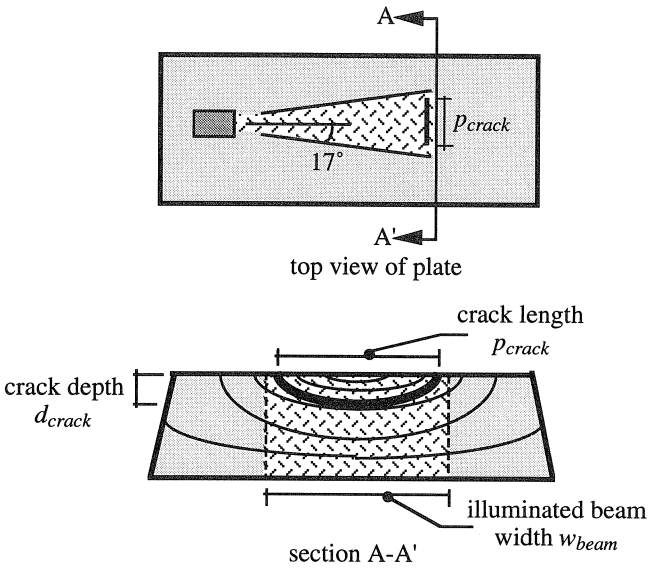

Fig. 4.20. Beam width of 70° probe at crack.

The simplified model adapts to the probe width limitation by including crack length as a separate, independent variable. A rectangular crack shape is assumed for the crack shape and when $p_{crack} < w_{beam}$ the energy increases in proportion to p_{crack} as well as the crack depth. When $p_{crack} > w_{beam}$ the energy increases only with crack depth. The crack surface area incorporates both d_{crack} and p_{crack} and provides a single variable with which to observe increases in E_{SAFT}.

Fig. 4.21 shows the measured E_{SAFT} values repeated from Fig.3.14 for pitch-catch testing. Three different apertures, 300–500 mm, 500–700 mm and 700–900 mm in (a)–(c) show how E_{SAFT} decreases with testing distance. Within each aperture, E_{SAFT} increases as the crack surface area increases. Fig. 4.21 also includes E_{SAFT} responses for corresponding simulated configurations found using the simplified, specular reflection ray model. As with the measured values, the modeled curve looks at relative increases in E_{SAFT} with the initial crack size at the 0 dB level.

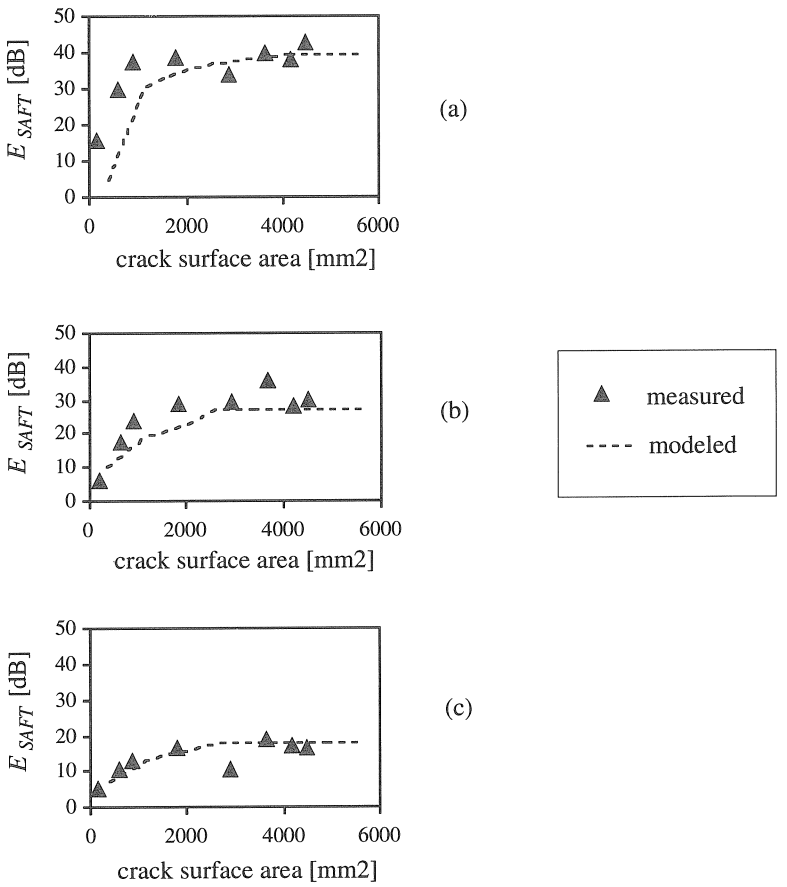

Fig. 4.21. Measured and modeled pitch-catch testing of a 40 mm plate. SAFT image energy, E_{SAFT}, versus crack surface area (a) synthetic aperture with receiver scanning from 300–500 mm, (b) aperture at 500–700 mm, (c) aperture at 700–900 mm.

The form and magnitudes of the modeled curves show excellent agreement with measured E_{SAFT} values. At longer testing distances (Fig. 4.21b and c) the model correctly predicts lower increases in energy resulting from longer wave paths and directional constraints of the probes. Within each aperture the model also provides a very good estimate

of the increase in energy resulting from the growing crack. The bend in the modeled energy curve results from the probe beam width limitation. Both the measured data and the modeled curve clearly show this phenomenon.
In the testing range of 300–500 mm (Fig. 4.21a) smaller crack sizes give higher measured E_{SAFT} values than expected from the model. At close range, the non-specular reflections contribute more to the reflected energy than at longer distances. Probes at close range can receive more non-specular response than when positioned farther away. The wave path in the SAFT image therefore contains more non-specular energy with a small defect tested at close range. In fact, close range SAFT-imaging relies on this non-specular field to obtain higher depth resolution. (Lorenz 1991)

4.4.3 Discussion of scan modeling results

The model of defect testing developed in this chapter uses a simplified source. Having finite length and continuous distribution of points along the interface, the source is assumed to act uniformly with a Dirac δ function. The source does not include the spatial and temporal characteristics of an angled probe, $A(x)$ and $t(x)$. Assumptions of specular reflection limit the model to testing of normally-oriented, smooth cracks. These types of fatigue cracks, while commonly occurring in practice, enable the simplification of modeling only the specular reflection in the wave field. Reflections from rough or obliquely-oriented defects require the addition of a crack model.
For a smooth, oblique crack, the largest amount of energy will still result from a perfect reflection, however the reflected wave does not return at the same angle as the angle of incidence upon the crack. In this case, the model must separately consider paths to and from the crack. The crack orientation determines the direction of the reflected path. For a rough defect, the scattered ray paths may account for most of the reflected energy rendering the model, with its specular crack reflection assumption, inappropriate. The scattered return paths from the crack also require separate consideration from the incident paths.
For the same reason, the specular reflection model only applies to very limited pulse-echo testing configurations. Because of the single probe configuration, pulse-echo testing relies on scattering at the defect to provide a return path to the same location as the send probe. Pulse-echo testing also requires separate consideration for the paths to and from a crack.
A more complex model requires consideration of the crack as a series of point sources. Fig. 4.22 shows a ray model of pulse-echo testing using point sources to represent the crack. As in SAFT-imaging, the model looks at a grid of points in the area of the defect. Each grid point has a corresponding arrival time and amplitude. In the presence of a reflector at the grid point, a return path registers a response at the receiver as if a point source existed at the mesh point. A point source simulates a reflector at the grid point with an initial travel time and amplitude based on the incident path to the grid point. The response at the receiver results from both the incident and reflected propagation paths. Modeling of the crack length would necessitate a three-dimensional model of the test system. This thesis does not include calculations for this detailed crack model.

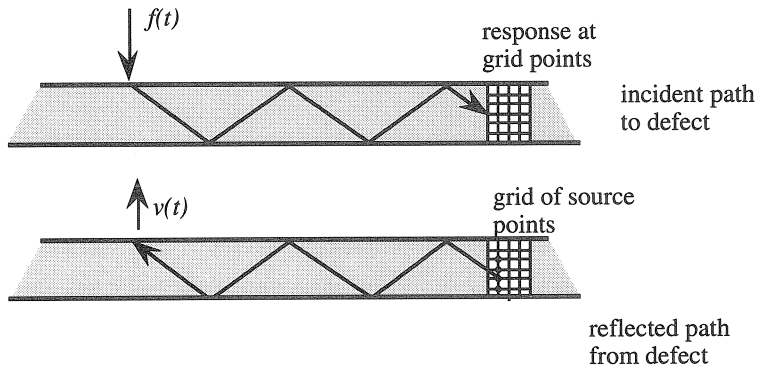

Fig. 4.22. Separately modeled incident and reflected paths using a defect as a point source.

Normal incidence of the wave field onto a planar defect permits the simplification of the wave field with a two-dimensional representation. This configuration has sufficient sensitivity to follow crack growth only when the length of the crack is smaller than the beam width of the illuminating probe. When the crack grows longer than the beam width there is insufficient dynamic range in the SAFT image energy to follow increases in crack depth from long testing distances. Sensitivity to crack growth for cracks larger than the beam width can only be measured with three-dimensional test configurations, thus scanning in the transverse direction or using multiple probes in the transverse direction.
The 2–5 MHz frequencies used in testing result in temporally discrete arrivals of the different waves. In modeling the testing process with ray theory, we take advantage of the discrete wave paths by finding the response exclusively from one wave path. SAFT-imaging uses only one ray path in an image. Modeling SAFT-imaging allows the elimination of all other rays from consideration. Other rays do not contribute to the SAFT image. This is the feature of using ray theory to model SAFT-processing results.
SAFT-processing eliminates the need for an extended probe model to verify the presence of a defect. The most important factor in SAFT-processing of data is a consistent pulse response from successive testing positions. An extended probe model only increases the accuracy of a single response when modeling wave propagation in a plate. In the simulation of SAFT-processing, accuracy of a single response is less important than consistency between adjacent positions. Unless a full crack model is used, an extended probe model does not help in modeling SAFT. SAFT can be simulated without a probe model. This is another feature of using SAFT to verify the location of defects.

4.5 *Conclusions*

This chapter develops a ray theory-based calculation model for long-distance testing of defects. A simplification of the model applies to the detection of normally-oriented, smooth cracks in pitch-catch testing. The simplified model compares very well to measurements from a real fatigue crack with normal orientation.

Modeling a single response from long-distance through-transmission measurements, i.e. without the presence of a defect, requires a detailed model of the source. Laser interferometry measurements enable the formulation of an accurate probe model. Measured through-transmission response is accurately simulated with the ray theory response using the probe model. Directionality of an angled probe is also accurately simulated with the model. The most critical component of the model in determining directionality of a probe is the projected speed of the incident *P*-wave upon the probe-steel interface.

To study the relationship between the reflected wave field and crack growth, a simplified model is developed which considers only specular reflection from the crack. The simplified model reduces computation time at the expense of comparing relative changes in energy rather than total energy reflected from a defect. This renders the simplified model appropriate for applications where periodic testing is possible.

In the testing of a normally-oriented crack, there is good agreement between experimental and simulated values of SAFT image energy, E_{SAFT}. The simplified model correctly predicts increases in E_{SAFT} even at testing distances up to 900 mm. A more complex model is described that could be used to determine the response from cracks that do not fall within the limitations of the simplified model.

5 Conclusions

The goal of this work is to develop a hybrid monitoring/inspection method whereby large areas of a structures can be evaluated with reasonable sensitivity. The sensitivity required is determined by the application. At this time, further development of the technique is dependent on the potential application.

The method developed, long-distance ultrasonic testing, can be used to inspect and monitor. It uses existing ultrasonic techniques together with ray theory modeling to evaluate sections in steel up to 1.0 m away. On large civil structures with members thicknesses of h = 25 mm–40 mm, this is equivalent to a testing distance of $25h$–$40h$. Long-distance capabilities are of particular interest for assessment of areas difficult to access by other testing methods. The same capabilities are also useful in economically assessing larger areas of a structure than normally found in inspection. Processing of ultrasonic signals from this distance permits detection and location of defects as small as 75 mm^2, comparable to the sensitivity of present inspection methods. When combined with analytical modeling, this method provides sufficient sensitivity to follow crack initiation and growth.

The advantage of long-distance testing is that detection and location of small defects is possible while large areas are evaluated. Crack growth can be followed using analytical calculations instead of experimental comparisons. The technique is intended as a testing method wherein detailed characterization is not expected; rather, the detection and/or growth of defects is of primary importance. If long-distance testing leads to the conclusion that better characterization is necessary then any localized inspection method can be used as a follow-up.

With this technique, complicated configurations and changes in cross-section are more difficult to process and model than with close-range ultrasonic methods. While it is not

impossible to model complex geometry's, more time is required before processing begins. Tests so far assume favorable orientation of defects. At this time, detection and location with this method is limited to defects whose plane is oriented normal to the axis of the testing probe. One limitation lies in the size of the cross-section. This method has only been tested on members with thicknesses from 20 mm–40 mm.
The experimental and analytical work in this study have yielded contributions to the knowledge in four areas of ultrasonic non-destructive testing of thick steel members:

- A better understanding of the mechanisms behind the components important to long-distance ultrasonic testing is provided by this work. In Chapter 2 known attenuation relationships are combined to model the wave propagation from an angled probe. These attenuation models show excellent agreement with measurements from a 70° probe. SAFT-imaging of measurements from 1.0 m away is shown in Chapter 3 to correctly locate a 75 mm^2 defect. Neither pitch-catch nor pulse-echo probe configurations can give depth characterization of a defect from this distance.
  Laser interferometry measurements presented in Chapter 4 provide a new method of deriving a multiple point source model of the angled probe. These measurements show that despite the lack of shear transfer from a probe to a test specimen, an angled wave is generated in the specimen through the spatial projection of the angled wave front and the resultant linear time delay of the wave as it transfers across the probe-specimen interface.

- Existing ultrasonic testing techniques may be used from distances up to 1.0 m ($25h$–$40h$) with little loss in detection and location capabilities. This is in contrast to present ultrasonic testing where localized testing occurs up to approximately 0.3 m ($7.5h$–$12h$) away. To evaluate 1.0 m of plate distance, manual or automated scanning near the inspection area is used. This work shows how 1.0 m of plate can be inspected from one set of measurements taken at one location. For certain applications, this is an economical alternative to present detection methods.

- Analytical modeling can mitigate the loss in characterization which accompanies inspection from long distances. In applications where more information than just detection and location are required, modeling can help track defect growth. By modeling possible defect sizes, a comparison of the model to measurement can estimate the severity of the defect. A similar approach is used in the characterization of defects with existing monitoring methods. Present inspection methods, however, generally do not use analytical modeling to characterize defects. The long-distance method developed in this work requires the use of modeling to interpret the waveforms. This analysis provides a powerful tool in the characterization of defects.

– A monitoring technique is proposed whereby sensitivity to small defects is much higher than with present monitoring techniques. The testing area with this technique is considerably smaller than those of other monitoring methods such as acoustic emission and vibration testing. When comparing present inspection and monitoring techniques, there is a tradeoff between sensitivity and the economy of a large testing area. This method attempts to balance the tradeoff between sensitivity and the size of the testing area, thus the term "hybrid" in its description.

Acknowledgement

This work has been supported by the Technology Foundation (STW) in the Netherlands.

References

BREEUWER, R., D. J. CHINN (1993). "Optoacoustic characterization of piezoelectric transducers", in *Review of Progress in Quantitative Nondestructive Evaluation*, Brunswick, Maine, Plenum Press (13, to be published).

CHINN, D. J. (1989), "Integrity assessment of offshore structures" Delft University of Technology, Report:25.2-89-1-13.

CHINN, D. J. (1990), "Long-Distance Ultrasonic Testing of Thick Steel Plates" Technology Foundation of the Netherlands (STW).

CHINN, D. J., DIETERMAN, H. A. (1992). "Generalized ray theory and its application to long-distance ultrasonic testing", in *International Union of Theoretical and Applied Mechanics Symposium on Inverse Problems*, Tokyo, Springer-Verlag.

CHINN, D. J. (1992). "Long-distance ultrasonic testing of welded steel connections: Comparison of theory to experiment", in *EUROMECH 295: Wave Processes in Machinery and Structures*, Nizhny Novogorod, Russia.

CHINN, D. J., H. A. DIETERMAN (1991). "Defect imaging using long-distance ultrasonic testing", in *Review of Progress in Quantitative Nondestructive Evaluation*, Brunswick, Maine, Plenum Press (11).

CHINN, D. J., H. A. DIETERMAN, R. BREEUWER (1993). "Modeling an angled probe using laser interferometry surface measurements", in *Review of Progress in Quantitative Nondestructive Testing*, Brunswick, Maine, Plenum Press (13, to be published).

COOPER, G. R., M. C.D. (1971). *Probabilistic Methods of Signal and System Analysis*, New York, Holt, Rinehart and Winston.

DOCTOR, S. R., T. E. HALL, L. D. REID (1986). "SAFT-the evolution of a signal processing technology for ultrasonic testing", *NDT International* 19 (3).

GENERAZIO, E. R. (1985). "The role of the reflection coefficient in precision measurement of ultrasonic attenuation", *Materials Evaluation* 43 (July).

HSU, N. N. (1985), "Dynamic Green's Functions of an Infinite Plate - A Computer Program" National Institute of Standards and Technology, USA:NBSIR 85-3234.

JOHNSON, J. (1982). "Parameter study of synthetic-aperture focusing in ultrasonics", in *Review of Progress in Quantitative Non-destructive Evaluation*, Plenum Press (1).

KRAUTKRÄMER, J., H. KRAUTKRÄMER (1990). *Ultrasonic Testing of Materials*, Berlin, Springer-Verlag(4th).

KÜHN, G. J., A. LUTSCH (1961). "Elastic wave mode conversion at a solid-solid boundary with transverse slip", *J. Acoustical Society of America* 33 (7).

LANGENBERG, K. J. (1987). "Applied Inverse Problems for Acoustic, Electromagnetic and Elastic Wave Scattering", in *Basic Methods of Tomography and Inverse Problems*. Bristol, Adam Hilger.

LANGENBERG, K. J., M. BERGER, T. KREUTTER, K. MAYER, V. SCHMITZ (1986). "Synthetic aperture focusing technique signal processing", *NDT International* 19 (3).

LEPERT, P., CHAY, M., HEAS, J.Y., NARZUL, P. (1980). "'Vibro-Detection' applied to offshore platforms", in *Offshore Technology Conference*, Houston.
LORENZ, M., VAN DER WAL, L.F., BERKHOUT, A.J. (1991). "Ultrasonic imaging with multi-SAFT", *Nondestructive Testing and Evaluation* 6.
LORENZ, M. (1993). *Ultrasonic Imaging for the Characterization of Defects in Steel Components*, Dissertation: Delft University of Technology, ISBN 90-90006160-6.
MCGILLEM, C. D., G. R. COOPER (1974). *Continuous and Discrete Signal and System Analysis*, New York, Holt, Rinehart and Winston.
OGILVY, J. (1988). "Computer simulation of acoustic wave scattering from rough surfaces", *J. Physics, D: Applied Physics* 21.
PAO, Y. H. (1977). "The generalized ray theory and transient responses of layered elastic solids", in *Physical Acoustics*. New York, Academic Press.
PROCTOR, T. M., F. R. BRECKENRIDGE, Y. H. PAO (1983). "Transient waves in an elastic plate: Theory and experiment compared", *J. Acoustical Society of America* 74 (6).
RAVENSCROFT, F. A., K. NEWTON, C. B. SCRUBY (1991). "Diffraction of ultrasound by cracks: comparison of experiment and theory", *Ultrasonics* 29 (Jan).
REDWOOD, M. (1960). *Mechanical Waveguides*, London, Pergamon Press.
SEYDEL, J. (1982). "Ultrasonic Synthetic-aperture Focusing Techniques in NDT", in *Research Techniques in Nondestructive Testing Vol. VI*. London, Academic Press.
TERPSTRA, S., J. P. PASMA, G. P. C. VAN WOERKOM (1989). "Monitoring heights of defects in welds using the ultrasonic time-of-flight diffraction technique", in *12th World Conference on Non-Destructive Testing*, Amsterdam, Elsevier.
VAN VLACK, L. H. (1977). *Elements of Material Science and Engineering*, Addison-Wesley(3rd).
VIKTOROV, I. A. (1967). *Rayleigh and Lamb Waves, Physical Theory and Applications*, New York, Plenum Press.
VROOMAN, H. A. (1991). *Quantitative analysis of interferograms*, Dissertation: Delft University of Technology, ISBN 90-6275-718-9.
WÜSTENBURG, H., E. SCHULZ (1977). "The influence of membrane size and form on the sound field of angle probes", in *Conference on the evaluation and calibration of ultrasonic transducers*, London, IPC Business Press.